JOURNAL OF THE ROYAL SOCIETY Interface

CrossMark click for updates

J. R. Soc. Interface (2012) **9**, 2563–2580
doi:10.1098/rsif.2012.0191
Published online 9 May 2012

Structure and optical function of amorphous photonic nanostructures from avian feather barbs: a comparative small angle X-ray scattering (SAXS) analysis of 230 bird species

Vinodkumar Saranathan[1,5,*,†], Jason D. Forster[2,5], Heeso Noh[3,5], Seng-Fatt Liew[3,5], Simon G. J. Mochrie[3–5], Hui Cao[3–5], Eric R. Dufresne[2,4,5] and Richard O. Prum[1,5,6,*]

[1]*Department of Ecology and Evolutionary Biology and Peabody Museum of Natural History,* [2]*Department of Mechanical Engineering and Materials Science,* [3]*Department of Applied Physics,* [4]*Department of Physics, and* [5]*Center for Research on Interface Structures and Phenomena (CRISP), Yale University, New Haven, CT 06520, USA* [6]*Donostia International Physics Center (DIPC), 20018 Donostia-San Sebastian, Spain*

Non-iridescent structural colours of feathers are a diverse and an important part of the phenotype of many birds. These colours are generally produced by three-dimensional, amorphous (or quasi-ordered) spongy β-keratin and air nanostructures found in the medullary cells of feather barbs. Two main classes of three-dimensional barb nanostructures are known, characterized by a tortuous network of air channels or a close packing of spheroidal air cavities. Using synchrotron small angle X-ray scattering (SAXS) and optical spectrophotometry, we characterized the nanostructure and optical function of 297 distinctly coloured feathers from 230 species belonging to 163 genera in 51 avian families. The SAXS data provided quantitative diagnoses of the channel- and sphere-type nanostructures, and confirmed the presence of a predominant, isotropic length scale of variation in refractive index that produces strong reinforcement of a narrow band of scattered wavelengths. The SAXS structural data identified a new class of rudimentary or weakly nanostructured feathers responsible for slate-grey, and blue-grey structural colours. SAXS structural data provided good predictions of the single-scattering peak of the optical reflectance of the feathers. The SAXS structural measurements of channel- and sphere-type nanostructures are also similar to experimental scattering data from synthetic soft matter systems that self-assemble by phase separation. These results further support the hypothesis that colour-producing protein and air nanostructures in feather barbs are probably self-assembled by arrested phase separation of polymerizing β-keratin from the cytoplasm of medullary cells. Such avian amorphous photonic nanostructures with isotropic optical properties may provide biomimetic inspiration for photonic technology.

Keywords: biophotonics; organismal structural colours; amorphous nanostructures; non-iridescence; single scattering; self-assembly

1. INTRODUCTION

Structural colours are prevalent in nature, and generally produced by the selective scattering and reinforcement of specific bands of wavelengths from biophotonic nanostructures with variations in refractive index on the order of visible wavelengths of light [1–5]. Like photonic crystals [6], biophotonic nanostructures vary in nanostructure in either one, two or three dimensions (figure 1*a–c*). However, they may also vary in whether they have long-range, crystalline periodicity, or only short-range (nearest neighbour), structural correlations [1–5] (figure 1*d–f*). The latter referred to as quasi-ordered or amorphous biophotonic nanostructures are characterized by unimodal

*Authors for correspondence (vinod.saranathan@zoo.ox.ac.uk; richard.prum@yale.edu).
†Present address: Edward Grey Institute of Field Ornithology, Department of Zoology, University of Oxford, South Parks Road, Oxford OX1 3PS, UK and Linacre College, St Cross Road, Oxford OX1 3JA, UK.

Electronic supplementary material is available at http://dx.doi.org/10.1098/rsif.2012.0191 or via http://rsif.royalsocietypublishing.org.

Received 9 March 2012
Accepted 17 April 2012

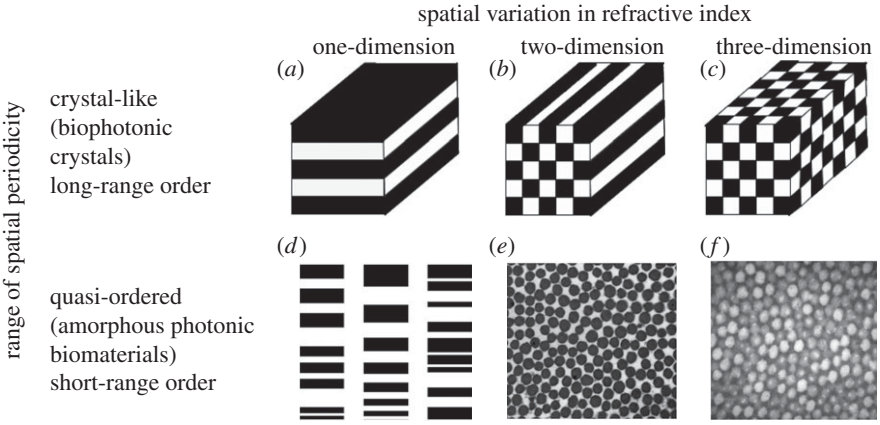

Figure 1. A classification of biophotonic nanostructural diversity based on the dimensionality of spatial variation in refractive index and its range of periodicity. (*a*–*c*) One-, two- and three-dimensional biological photonic crystals with long-range periodic order in refractive index modulations (after Joannopoulos [6]). (*d*) A chirped lamellar stack, a one-dimensional quasi-ordered nanostructure with short-range spatial periodicity (currently unknown in birds; after Parker [2]). (*e*) TEM cross section of a two-dimensional amorphous or quasi-ordered nanostructure with short-range order comprising of parallel collagen fibres in a mucopolysaccharide matrix from the green tongue of magnificent bird-of-paradise (*Cicinnurus magnificus*, Paradisaeidae). (*f*) TEM cross section of a three-dimensional amorphous or quasi-ordered nanostructure of β-keratin and spheroidal air vacuoles from the spongy medullary cells of the azure blue crown feather barbs of male Blue-crowned Manakin (*Lepidothrix coronata*, Pipridae) with short-range quasi-periodic order.

distributions of scatterer size and inter-scatterer spacing, and a notable lack of any underlying periodicity beyond the span of a few nearest neighbours (figure 2*e*,*f*) [3,7–9].

Vivid, non-iridescent structural colours in bird plumages (figure 2*b*,*c*) are taxonomically widespread and appear to have evolved numerous independent times during the evolutionary history of birds in many ecologically diverse lineages [3,9]. They constitute an important component of the phenotype of many birds, and are frequently used in intraspecific communication and camouflage (reviewed in [10,11]). Because the optical properties of biophotonic materials are intimately tied to the underlying nanostructures, a precise mechanistic characterization of organismal structural colour production is critical to study how such biological signals evolve.

The non-iridescent structural colours of avian feather barbs are generally produced by three-dimensional, quasi-ordered nanostructures composed of β-keratin (refractive index, $n = 1.58 \pm 0.01$; [12]) and air in the medullary cells of feather barbs (reviewed in [3]). The colours so produced do not appreciably change in hue with changes in angle of observation under natural lighting because back-scattered light dominates under such conditions [13]. Spongy barb nanostructures have been directly examined in only a relatively small number of avian taxa (approx. 28 species from 16 families [3]), but typically known to occur in one of two distinct morphologies. The *channel-type* nanostructures are characterized by a tortuous, interconnected bicontinuous network of air channels and β-keratin bars of similar widths and shapes (figure 2*e*) [3,7–9,14]. The *sphere-type* nanostructures consist of a quasi-ordered close packing of spheroidal air cavities that are separated by β-keratin walls and frequently interconnected by tiny air passages (figure 2*f*). However, D'Alba *et al.* [15] recently discovered a unique two-dimensional, medullary, feather barb nanostructure comprising bundles of parallel, quasi-ordered, β-keratin nanofibres in air that is responsible for the non-iridescent blue colour of Blue Penguin (*Eudyptula minor*, Spheniscidae).

1.1. Small angle X-ray scattering (SAXS)

Previous research using Fourier analysis of two-dimensional transmission electron microscopy (TEM) images of amorphous barb nanostructures has documented their isotropic quasi-order from their ring-shaped two-dimensional Fourier power spectra [3,7–9,16]. Fourier analyses of TEM images were sufficiently accurate to falsify the century-old, single particle (Tyndall or Rayleigh, and Mie) scattering hypotheses, which assumed that the colour comes from wavelength-dependent light scattering properties of isolated, spatially uncorrelated scatterers [3,7–9,16]. But two-dimensional Fourier power spectra of TEM images lack the resolution to account for the variation in reflectance features of these complex three-dimensional nanostructures [3,7–9,17–20]. They also suffer from artefacts owing to EM sample shrinkage and others related to analysing a finite-thickness (approx. 90 nm), low-resolution, two-dimensional slice of a three-dimensional nanostructure, such as aliasing, binning, etc. Nevertheless, most studies of avian structural colours have used two-dimensional electron microscopy to characterize their underlying three-dimensional biophotonic nanostructures [3,7–9,14, 17–19,21–25]. However, fundamental uncertainty remains about the exact organization of these three-dimensional amorphous feather barb nanostructures. Shawkey *et al.* [26] recently performed three-dimensional electron tomographic reconstruction of the channel-type barb nanostructure in blue rump feathers of Eastern Bluebird (*Sialia sialis*), and made a reasonable prediction of the optical reflectance from the azimuthal average of the three-dimensional Fourier transform of the tomogram. However, sample shrinkage and tomographic distortion limited the accuracy of structural and optical analyses [26,27].

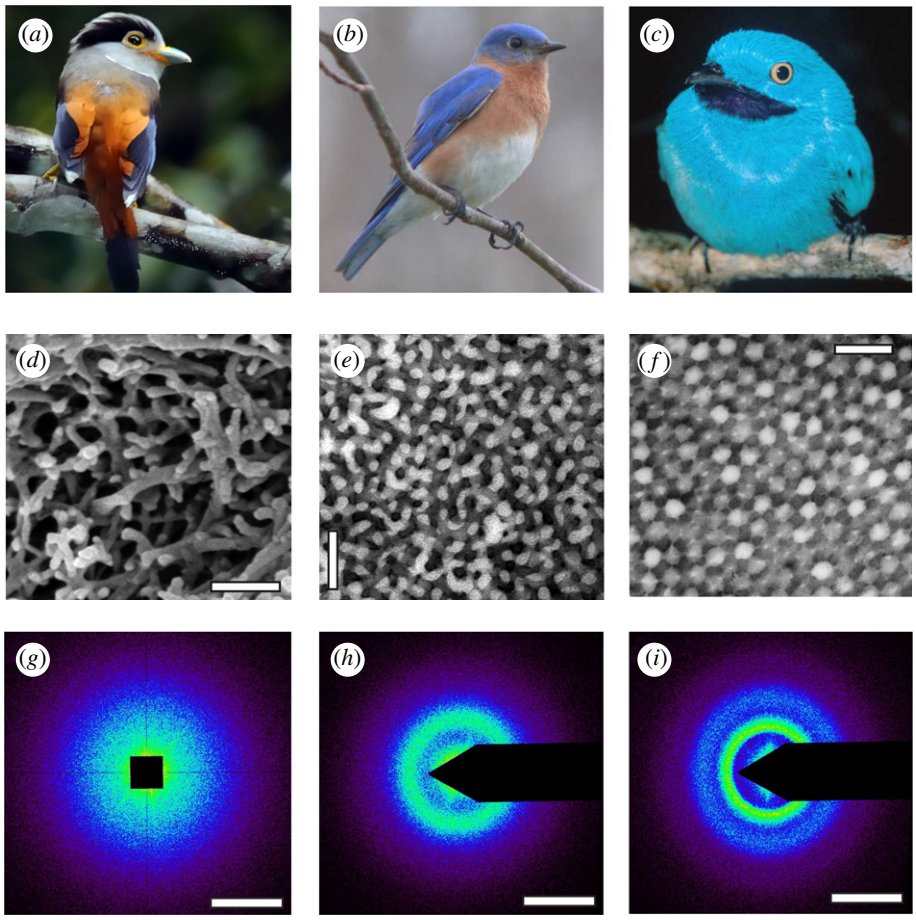

Figure 2. Diversity of non-iridescent feather barb structural colours in birds and morphology of their underlying three-dimensional amorphous photonic nanostructures with short-range quasi-periodic order. (*a*) Female Silver-breasted Broadbill (*Serilophus lunatus*, Eurylaimidae). (*b*) Male Eastern Bluebird (*S. sialis*, Turdidae). (*c*) Male Plum-throated Cotinga (*Cotinga maynana*, Cotingidae). (*d*) SEM image of a rudimentary nanostructure with a very thin layer (1 μm or less) of a disordered network of spongy β-keratin bars present at the periphery of the medullary barb cells from the pale blue-grey primary coverts of *S. lunatus*, (*e*) TEM image of a channel-type β-keratin and air nanostructure from royal blue back contour feather barbs of *S. sialis*. (*f*) TEM image of a sphere-type β-keratin and air nanostructure from the dark turquoise blue back contour feather barbs of *C. maynana*. (*g–i*) Representative two-dimensional small-angle X-ray scattering (SAXS) diffraction patterns for the rudimentary, channel- and sphere-type feather barb nanostructures in (*d–f*), respectively. The SAXS patterns for both channel- and sphere-type nanostructures exhibit ring-like features that demonstrate the isotropy and short-range spatial periodicity of these nanostructures, whereas the rudimentary barb nanostructure shows a diffuse, disc-like pattern. The false colour encoding corresponds to the logarithm of the X-ray scattering intensity. Scale bars: (*d*) 250 nm; (*e*,*f*) 500 nm; (*g–i*) 0.05 nm^{-1}. Photo credits: (*a*) Yiwen Yiwen (image in the public domain); (*b*) Ken Thomas (image in the public domain); and (*c*) Thomas Valqui (reproduced with permission).

Here, we use synchrotron small angle X-ray scattering (SAXS) to quantitatively characterize the nanostructure and optical function of a large sample of structurally coloured feathers with spongy barb nanostructures, from across the phylogeny of birds. We examine the nanostructure and optical properties of 297 distinctly coloured feathers from 230 species belonging to 163 genera in 51 avian families (see electronic supplementary material, table S1). SAXS is a precision structural tool routinely used in material science to directly measure bulk structural correlations in complex nanostructured morphologies [28–31]. SAXS enables a direct experimental measurement of the two-dimensional projection of the three-dimensional Fourier transform of the scattering structure (figure 3) with essentially no sample preparation, allowing for rapid throughput inconceivable with electron microscopy methods [29,31,32]. The azimuthal average of the SAXS pattern gives the X-ray scattering intensity as a function of q, the scattering wavevector, or spatial frequency of variation in electron density (which is a proxy for variation in refractive index). The SAXS patterns resolve spatial correlations of dimensions $2\pi/q$ that range from a few tens to several hundred nanometres (figures 3–5). X-rays also interact only weakly with soft biological tissues because of the relatively low electron density of biological media [28–31,35]. Hence, SAXS provides single scattering data that are highly suited to quantitatively predict the interactions of visible light with the nanostructure without artefacts resulting from multiple scattering. Recently, we applied SAXS to a few species with non-iridescent feather barb structural colours—Eastern Bluebird (*S. sialis*), Purple-throated Cotinga (*Cotinga maynana*), Blue Cotinga (*Cotinga cotinga*), Asian Fairy Bluebird (*Irena puella*), Indian Roller (*Coracias benghalensis*) and Blue Penguin (*Eudyptula minor*)—and successfully modelled the directional light scattering properties of

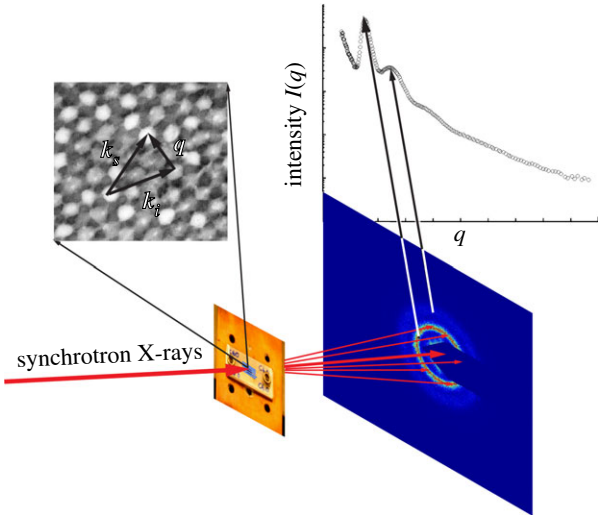

Figure 3. Experimental schematic for SAXS experiments on feather barb nanostructures. A small (approx. 50 mm^2) sample of the distal pennaceous portion of the feather vane is shown affixed to cover a 3 mm diameter hole on an aluminium block, which is then mounted in a plane perpendicular to the incident X-ray beam. The two-dimensional SAXS diffraction patterns for both channel- and sphere-type nanostructures exhibit ring-like features. Exploiting the circular symmetry of the SAXS diffraction patterns, the scattering intensity (I) is azimuthally averaged as a function of q to obtain scattering profiles, where the peaks correspond to the rings observed in the respective two-dimensional diffraction patterns. The scattering wavevector q measures the momentum transfer or the magnitude and direction of the scattering of incident photons (k_i into k_s) as a result of constructive interference from structural correlations of size $2\pi/q$ within the nanostructure.

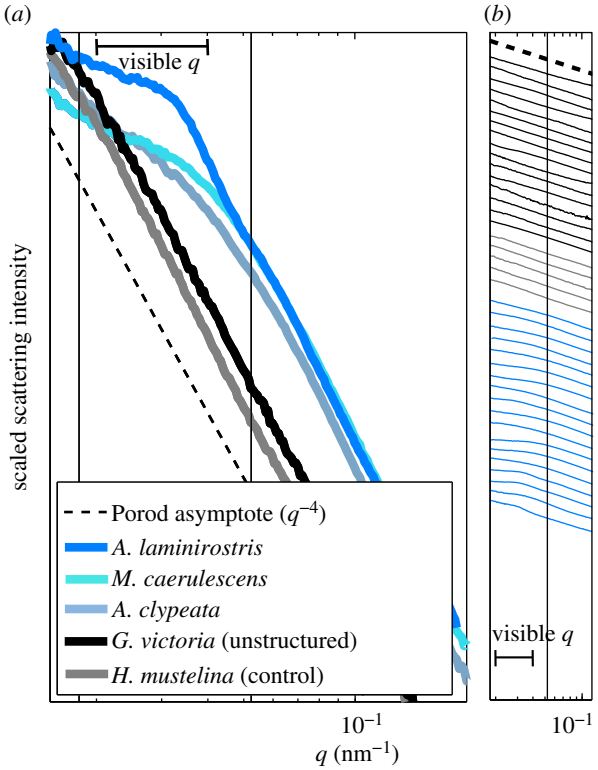

Figure 4. SAXS structural diagnosis of weakly structured, control and unstructured feather barbs. (*a*) Representative azimuthal SAXS profiles for the rudimentary sphere-type nanostructure ('structured*', electronic supplementary material, table S2) in *A. laminirostris* (Ramphastidae), and the rudimentary channel-type nanostructures ('structured', see electronic supplementary material, table S2) in *Melanotis caerulescens* (Mimidae) and *Anas clypeata* (Anatidae) as well as unstructured feather barbs from *Goura victoria* (Columbidae) and *Hylocichla mustelina* (Turdidae). The azimuthal profiles are normalized to one along the intensity axis for ease of comparison. (*b*) The azimuthal SAXS profiles for 18 weakly structured (blue lines), five control (grey lines) and 16 unstructured feather barbs (black lines) on a semi-log scale. The azimuthal profiles are vertically displaced along the intensity axis for clarity. The azimuthal scattering profiles of the control feathers, many purple, magenta and bright white feathers as well as several marginally blue-grey (black lines) feathers did not deviate from Porod's Law even at low q (<0.04 nm^{-1}). Thus, these feathers do not possess any underlying barb nanostructure, ruling out any contribution of constructive interference to their observed colours. The azimuthal SAXS profiles from feathers with mainly slaty blue-black to pale greyish-blue colours show slight to moderate deviations from Porod's Law at low q, with these features resembling a shoulder rather than a peak. Nevertheless, the spatial correlations that these feather barbs do possess appear to be at the appropriate length scales to be able to produce visible structural colours through interference. (*a*,*b*) The thick horizontal line indicates the range of spatial frequencies relevant for avian visible structural colour production.

their underlying amorphous photonic nanostructures [13,15,36–38].

1.2. Self-assembly by phase separation

Macro-molecular self-assembly through phase separation is a fundamental property of soft condensed matter systems [28]. The stability of a molecular mixture is determined by its temperature, the strength of intermolecular interactions (χ) and the relative volume fractions of the component materials. At lower temperatures and intermediate volume fractions, a mixture may become unstable and can proceed to unmix by one of two fundamental physical processes [28]. Phase separation of a completely unstable mixture can proceed via *spinodal decomposition* (SD), which usually produces a characteristic morphology of interconnected bicontinuous channels [39,40]. The observed fractal-like patterns or motifs begin at small length scales and spontaneously coarsen or thicken over time roughly maintaining the same average shape in a scale-independent fashion (self-similarity). By contrast, a meta-stable mixture can unmix through *nucleation-and-growth*, which proceeds via the development and subsequent coarsening of spherical droplets of the minority component [41,42]. Unlike SD, however, nucleation requires the crossing of an activation barrier. If nucleation is fast and growth, relatively slow, nearly identical (or monodisperse) spheres can form [43,44]. For simplicity, we have summarized here the morphologies observed during the classical phase separation of a simple binary fluid mixture. However, phase separation phenomenology should be modified to include nonlinear viscoelastic mechanisms when the two nascent phases have distinct rheological (i.e. mechanical) properties, such as in mixtures of a network-forming or polymerizing component and a fluid [45–47]. In this scenario, polymerizing proteins may form networks that resist

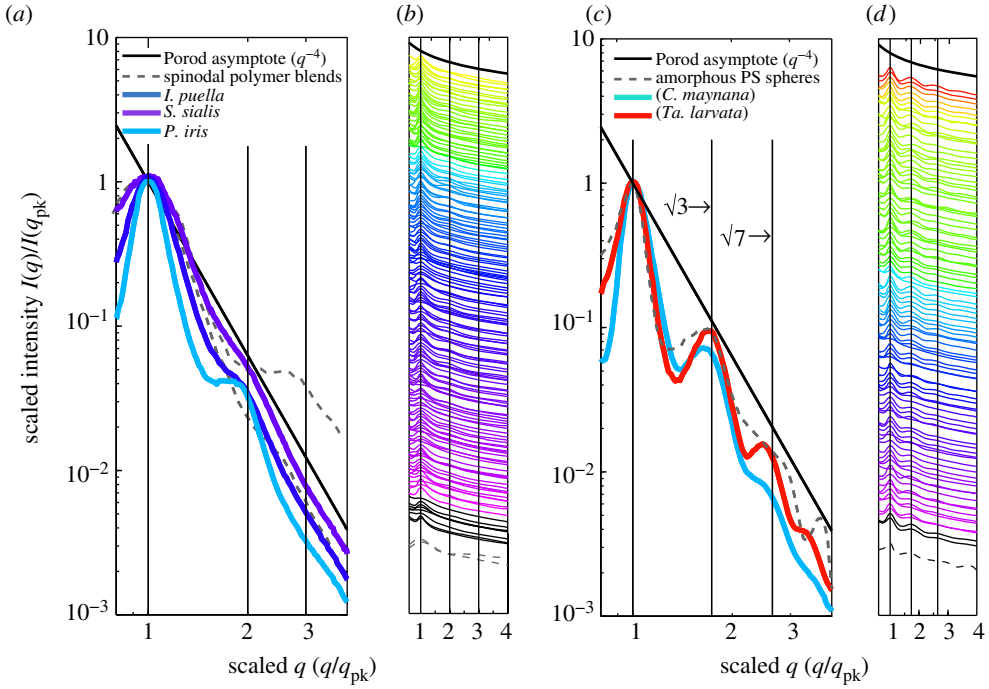

Figure 5. SAXS structural diagnosis of amorphous photonic nanostructures in feather barbs. (*a*) and (*c*) depict, respectively, representative normalized azimuthal SAXS profiles for channel-type nanostructures from *I. puella* (Irenidae), *S. sialis* (Turdidae), and *Pitta iris* (Pittidae) and sphere-type nanostructures from *C. maynana* (Cotingidae) and *Tangara larvata* (Thraupidae) on a log–log scale exhibiting clearly distinguishable structural differences. The azimuthal profiles are scaled to compare across different colours and nanostructural sizes. (*b*) and (*d*) show, respectively, scaled azimuthal SAXS profiles for 159 channel- and 96 sphere-type nanostructures on a semi-log scale. The colour of each profile is coded to the approximate colour of the corresponding feathers based on its primary optical peak hue (pure UV colours shown in black). These azimuthal profiles are vertically displaced along the *y*-axis for clarity. In addition to the primary peak, the channel-type nanostructures (*a*,*b*) either have a weak to a pronounced shoulder at approximately twice the dominant spatial frequency, $2^{*}q_{pk}$ or lack any other significant feature, while the sphere-type nanostructures (*c*,*d*) exhibit one or more pronounced higher-order scattering peaks in addition to the primary peak at ratios of approximately $\sqrt{3}$ and $\sqrt{7}$ times q_{pk}. The grey dashed lines in all figures plot the scaled experimental scattering profiles from two polymer mixtures undergoing spinodal decomposition [33,34] (*a*,*b*) and an amorphous film of self-assembled colloidal polymer spheres (*c*,*d*). The vertical lines at 1,2,3 (*a*,*b*) and at 1,$\sqrt{3}$ and $\sqrt{7}$ (*c*,*d*) are visual guides for the expected positional ratios for the SAXS peaks based on experimental observations of classical spinodal and nucleated, close-packed sphere morphologies, respectively.

coarsening while the solvent lacks such dynamic elasticity. Such viscoelastic processes lack self-similarity in the coarsening of domains, and are also hypothesized to dynamically self-arrest either owing to the cross-linking of networks or from the evaporation of solvent during phase separation [45–47].

Prum *et al.* [25] used TEM of serial sections to observe the development of channel-type nanostructure in the growing feather germ of parrot feathers. They found that these amorphous intracellular nanostructures develop spontaneously without any underlying biological template or prepattern of cytoskeletal fibres or membranes and thus evidently self-assembled. Furthermore, they pointed out that these nanostructures bear a qualitative similarity to morphologies self-assembled during SD. Later, based on the SAXS data from two species, Dufresne *et al.* [38] hypothesized that both channel and sphere nanostructures in birds could be self-assembled by arrested phase separation of filamentous β-keratin protein from the cellular cytoplasm. Further, they [38] proposed that the two classes of nanostructures, channel- and sphere-types, could possibly be self-assembled by SD and nucleation-and-growth mechanisms, respectively.

Here, we further test the hypothesis that constructive interference of light scattered by three-dimensional quasi-ordered photonic nanostructures is responsible for the non-iridescent plumage structural colours found in diverse avian lineages [3,8,9]. We also quantitatively compare the SAXS data from hundreds of feather nanostructures with experimental scattering data from self-assembled, synthetic soft condensed matter systems.

Using single scattering theory [8,13,16,48], we predict the optical reflectance of each nanostructure from the SAXS structural data and compare it with normal incidence optical measurements, and in addition perform angle-resolved spectrophotometry on a subset of the feathers. Further, we quantitatively explore the differences in the nanostructure and optical function of channel- and sphere-type barb nanostructures.

2. MATERIAL AND METHODS

2.1. Taxon sampling

We surveyed the birds of the world to identify all avian families and genera with probable non-iridescent structurally coloured barb colours (usually blues, violets, greens, etc.) from museum specimens and published illustrations (see electronic supplementary material, table S1). We cross-checked target species for the presence of

non-iridescent structural colours (peaked reflectance profiles) by visual inspection and optical spectrophotometry of museum skins. We sampled across the gamut of known structural hues including the near ultraviolet (visible to birds but not to humans), violet, blue, cyan and green, as well as saturated (peaked) yellow–red hues when they co-occur on birds with obvious barb structural coloration (blues and greens). We included feather samples of multiple plumage patches with different colours from the same species as well as differently coloured, but homologous patches from both sexes of sexually dichromatic species (see electronic supplementary material, table S1). We included in the sample some species with ambiguous blue–grey (e.g. *Polioptila caerulea, Pachyptila vittata*) and dull slate-coloured (e.g. *Brachypteryx montana*, *Rhyacornis fuliginosus*) feathers (see electronic supplementary material, table S1). We also sampled five 'control' feathers with eu- and phaeo-melanin, carotenoid pigments, and unpigmented matte white colour, chosen from the avian genera *Corvus*, *Hylocichla*, *Carduelis*, *Saltator* and *Larus* that should in theory lack any structural colour-producing barb nanostructure (see electronic supplementary material, table S2). In order to assess the variability of barb structural colour within and among individuals of a single species, we assayed feathers from multiple study skins of *S. sialis* and *C. maynana* (see the electronic supplementary material).

In total, including controls, we examined the nanostructure of 297 distinctly coloured feathers from 230 species belonging to 163 genera in 51 avian families (see electronic supplementary material, table S1). Feathers were obtained from study skins of the taxa of interest from Yale Peabody Museum of Natural History (New Haven, CT, USA), University of Kansas Natural History Museum and Biodiversity Research Center (Lawrence, KS, USA), American Museum of Natural History (New York, NY, USA), Natural History Museum at the Academy of Natural Sciences (Philadelphia, PA, USA), Harvard University Museum of Comparative Zoology (Cambridge, MA, USA) and University of Oxford Natural History Museum (Oxford, UK) (see electronic supplementary material, table S1). Immature individuals or specimens with obvious fading or degradation were avoided.

2.2. Small angle X-ray scattering

For SAXS data collection, small (approx. 50 mm^2) samples of the distal pennaceous portion of the feather vanes were affixed to an aluminium block using Super Glue (DuPont, Wilmington, DE, USA) over a 3 mm diameter hole. The block was mounted in a plane perpendicular to the incident X-ray beam as shown in the experimental schematic (figure 3). Pinhole SAXS data on two to three individual barbs per feather sample were collected in transmission geometry, at beamline 8-ID-I of the Advanced Photon Source, Argonne National Laboratories (Chicago, IL, USA). We used a 15 μm (Horiz. × Vert.) beam (1.68 Å, 7.35 keV, 50 × 0.2 s exposures, sample-detector distance 3.56 m, flux 2.7×10^9 photons s^{-1}). Beam size was minimized to sample as few spongy medullary cells as possible (they are typically approx. 10–15 μm^3 but vary with taxon [49]). The azimuthally averaged scattering profiles were calculated from the CCD-collected two-dimensional SAXS speckle diffraction patterns using the freely available Matlab-implemented software, XPCSGUI, developed by beamline 8-ID (http://8id.xor.aps.anl.gov/UserInfo/Analysis/) at 200 equal q-partitions, and with customized masks to filter out the beam stop [15,38,50]. SAXS data from the feathers of *Cittura cyanotis* and the yellow throat of *Psarisomus dalhousiae* (see electronic supplementary material, tables S1 and S2) were collected using a 7.35 keV beam (1.68 Å, 50 μm horizontal × 50 μm vertical, 9.24 m camera length, 50 × 0.1 s exposures) on a Pilatus2M detector at beamline I22 of the Diamond Light Source, Didcot, UK.

Biomimetic amorphous samples that closely mimic quasi-ordered arrays of a nucleation-and-growth structure were prepared by drop casting a 50 : 50 bidisperse mixture of 258 and 286 nm diameter polystyrene (PS) spheres [51]. SAXS measurements of biomimetic samples were carried out by sandwiching the sample in an aluminium sample holder between two pieces of 0.0025-inch (approx. 63.5 μm) thick adhesive Kapton tape, purchased from McMaster-Carr (Catalogue no. 7648A33). Light scattering data for phase-separating spinodal morphologies were obtained from Takenaka & Hashimoto [33] and Hayashi *et al.* [34].

2.3. Normal incidence and angle-resolved spectrophotometry

Normal incidence reflectance measurements were made from two or three different locations within each sampled plumage patch and averaged. Whenever possible, the same museum study skins that were sampled for the SAXS structural assays were used for the corresponding reflectance measurements. For 77 plumage patches, the original study skins were locally unavailable for spectrophotometry, and reflectance was measured from the individual feathers collected for SAXS assays (see electronic supplementary material, table S1). These feather-based reflectance measurements were essentially identical to those measured from other museum specimens of the same species. All measurements were made in relative darkness using an Ocean Optics S2000 (Dunedin, FL, USA) fibre optic spectrophotometer and an Ocean Optics DH-2000-BAL deuterium–halogen light source, following standard procedure [7–9]. The S2000 provides 2048 data points between 178 and 879 nm. In order to shield any ambient light and control the irradiance, the bifurcated fibre-optic cable was inserted into a probe holder. Reflectance was measured using normally incident light at a distance of approximately 6 mm from approximately a 3 mm^2 illuminated patch of the integument with a 500 ms integration time and calibrated using an Ocean Optics Spectralon matte white reflectance standard and with a matte black velvet cloth as dark reference.

We also conducted angle-resolved spectrophotometry in diffuse scattering geometry [13,36,37] on a smaller set of 22 individual feather samples with both channel-

and sphere-type nanostructures, to differentiate between double scattering versus pigmentary origin of the short-wavelength secondary reflectance features using the effects of angular dispersion, as well as to estimate the nanostructural parameters independent of the SAXS data. The bird feathers were mounted horizontally so that their axes were perpendicular to the rotation axis of a goniometer. Collimated white light from an Optics DH-2000-BAL deuterium–halogen light source was incident on the sample at normal incidence and with a spot size of approximately 1 mm. The scattered light was collected by a lens and focused onto an optical fibre connected to a spectrometer (Ocean Optics S2000). The spectral resolution was 1.5 nm and the angular resolution, determined mainly by the collection angle of the lens, was about 5°. To measure the scattered light, we fixed the feather sample and rotated only the detection arm, in which case, the illumination angle remained constant while the angle of observation changed. The measured spectra of scattered light were normalized by the incident source light spectrum after dark subtraction.

2.4. Electron microscopy

We followed standard specimen embedding procedures for TEM [7–9]. For scanning electron microscopy (SEM), longitudinally and cross-sectionally fractured feather barb samples were gold-coated and studied on a Hitachi SU-70 and a Philips XL 30 environmental SEM at a range of tilt angles.

2.5. Parametrization of small angle X-ray scattering structural data and optical reflectance spectra

The two-dimensional SAXS diffraction patterns for both channel- and sphere-type nanostructures exhibit ring-like features (figure 2*h*,*i*). Exploiting the circular symmetry of the SAXS diffraction patterns, we azimuthally integrated them using the XPCSGUI package after masking out the beam stop pixels, to obtain profiles of the scattered intensity as a function of scattering wavevector, $I(q)$, at 200 equal q-partitions or spatial frequency bins (figures 3–5). The peaks in the azimuthal profiles correspond to the rings observed in the respective two-dimensional diffraction patterns (figure 3). The azimuthally averaged profiles were deconvolved, or peak-fitted, to estimate the peak q value, intensity, and the full-width at half-maximum (FWHM) of the scattering peaks, using the freely available peak-fitting software, Fityk (v. 0.8.2; [52]) on a Windows platform. We used a Porod background (q^{-4} dependence; see §3 and figures 4–5) and the split-Pearson VII function with a Levenberg–Marquardt least square method to fit all the observed scattering features (peaks and shoulders) present in the azimuthal profiles. The Pearson VII function is a combination of Gaussian and Lorentzian (Cauchy) type peak profiles that is generally used to closely approximate X-ray scattering peaks [53,54]. The split-Pearson VII accommodates any asymmetry in peak shapes.

The unprocessed optical reflectance measurements were also similarly deconvolved to estimate the relevant optical peak parameters such as wavelength of peak reflectance, intensity and FWHM of the reflectance peak using Fityk. The FWHM characterizes the saturation of optical (reflectance) signals [55]. We used a constant background and a Gaussian or a split Gaussian function with a Levenberg–Marquardt least square method to fit all the observed spectral features (peaks and shoulders) present in the reflectance profiles. The split Gaussian function was used for asymmetrical peak profiles.

2.6. Small angle X-ray scattering single-scattering reflectance predictions

We used the azimuthally averaged SAXS structural spectra to directly predict the optical reflectance spectra of the respective amorphous barb nanostructures using single-scattering theory by mapping the SAXS intensity from wavevector or spatial frequency (q) to wavelength (λ) space [8,13,16,48,50]. This result follows from Bragg's Law, for under normal incidence of light and back-scattering geometry (the angle between incidence and observation, $\theta = 0°$), the scattering wavevector (q) and the wavelength of light (λ) are simply related as

$$\lambda = 2\left(\frac{2\pi}{q}\right) n_{\mathrm{avg}}, \tag{2.1}$$

where $2\pi/q$ is the average inter-scatterer or nearest-neighbour spacing D, and n_{avg} is the average or effective refractive index of the nanostructure [13].

2.7. Statistical analyses

Regression analyses were performed using the statistics toolbox of Matlab 2008a (The MathWorks Inc., Natick, MA, USA) and Minitab statistical software, release 16 (Minitab Inc., State College, PA, USA) running on a Windows platform. One-way ANOVA and general linear model tests for the statistical difference of the slopes and intercepts of two regression lines [56] were all performed in Minitab. The p-value for statistical significance was set at 0.05.

3. RESULTS

3.1. Comparative structural diagnoses of feather barb photonic nanostructures

Of the 297 feathers assayed in this study, the azimuthal scattering profiles of the 'control feathers' ($n = 5$) did not deviate from Porod's Law even at low q ($<0.04\ \mathrm{nm}^{-1}$) (figure 4, and electronic supplementary material, table S2). The scattering profiles of some feathers with longer-wavelength reflectance, including deep purple and magenta ($n = 9$), bright whites ($n = 3$) and some blue-grey feathers ($n = 4$) did not deviate from Porod's Law as well (figure 4 and electronic supplementary material, table S2). Porod's Law ($I(q) \propto q^{-4}$) is the 'null' expectation for the scattering from an unstructured material characterized by sharp interfaces or edges separating two media [31]. Thus, these 21 feathers do not

possess any underlying barb structure at optically relevant length scales ruling out any contribution of constructive interference to their observed colours.

The SAXS data from a further 18 out of 297 feathers (see electronic supplementary material, table S2) with slaty blue-black to pale greyish-blue colours, such as the primary coverts of the Silver-breasted Broadbill (*Serilophus lunatus*, Eurylaimidae; figures 2*a* and 4) exhibited diffuse, disc-like two-dimensional SAXS diffraction patterns (figure 2*g*). Their corresponding azimuthal averages showed slight to moderate deviations from Porod's Law at low q; these features resembled a shoulder rather than a peak (figure 4). Nevertheless, the spatial correlations of these feather barbs appear to be at the appropriate length scales to produce visible structural colours through constructive interference (figure 4). For 16 of these 18 feathers, the primary scattering feature could not be estimated with peak-fitting procedures (called 'structured', see electronic supplementary material, table S2).

We examined some of these slaty, blue-grey feathers with distinctive disc-like SAXS patterns using SEM. SEM images from two 'structured' species, *Serilophus lunatus* (Eurylaimidae) and *Melanotis caerulescens* (Mimidae), revealed a very restricted and thin layer (1 μm or less) of a disordered channel-like network of spongy β-keratin bars present at the periphery of the medullary barb cells (figure 2*d* and electronic supplementary material, S1c). All of these 16 'structured' species are closely related to other species known to possess the channel-type medullary barb nanostructures (figure 5*b* and electronic supplementary material, table S2). The two species for which the peaks could be estimated (called 'structured*', see electronic supplementary material, table S2) were the toucans *Andigena laminirostris* and *Pteroglossus viridis* (Ramphastidae). Other toucans have sphere-type nanostructures (figure 5*d* and see electronic supplementary material, table S2). SEM images of *A. laminirostris* revealed a very thin layer (1 μm or less) of hollow spheroidal concavities of highly variable sizes and shapes (highly polydisperse) in the spongy β-keratin at the periphery of the medullary cells (see electronic supplementary material, figure S1*d*). Thus, these blue-grey and slate-grey feathers characterized by diffuse, disc-like SAXS patterns possessed rudimentary and highly disordered versions of channel- ('structured') and sphere-type ('structured*') nanostructures, found in their close relatives.

The two-dimensional SAXS diffraction patterns of rest of the barb nanostructures assayed exhibit ring-like features that demonstrate strong nanostructural isotropy and short-range spatial periodicity (figure 2*h*,*i*). The azimuthally averaged scattering profiles display peaks that correspond to the rings observed in the respective two-dimensional diffraction patterns (figure 3). For comparison of feathers across different structural colours, nanostructural dimensions and scattering intensities, we normalized all azimuthal SAXS profiles by the primary peak spatial frequency (q_{pk}) and intensity ($I(q_{pk})$) (figure 5). In the high q region ($q > 0.1\ \mathrm{nm}^{-1}$), the SAXS profiles follow Porod's Law. However, at low and intermediate q values ($q < 0.1\ \mathrm{nm}^{-1}$), the azimuthal SAXS profiles of most barbs exhibit clearly distinguishable features that can be used to identify the barb nanostructures.

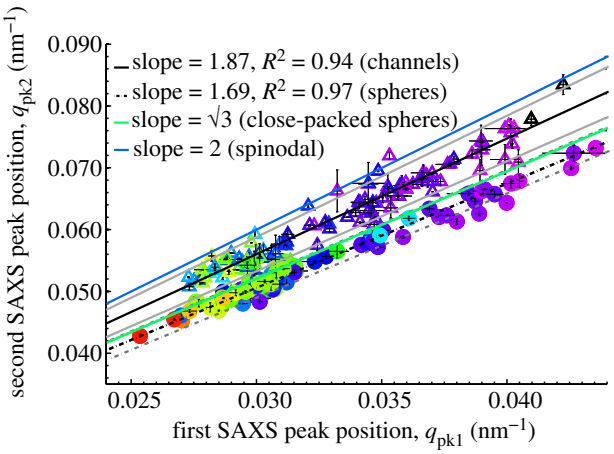

Figure 6. Regression plot of the first and second SAXS peaks of channel- (open triangles) and sphere-type (shaded circles) amorphous barb nanostructures. The colour of each triangle or circle is coded to the approximate colour of the corresponding feather (UV colours in black). The thin vertical and horizontal lines at each data point indicate the standard error of the mean (s.e.m). The solid blue and green lines with corresponding slopes of 2 and √3 indicate the expected positional ratios for the second SAXS peak based on experimental observations of spinodal and nucleated, close-packed sphere morphologies, respectively. The solid and dashed grey lines, respectively, indicate the 95% confidence interval of the regressions.

Of the remaining 258 feathers, 218 were readily classifiable into the two known classes of three-dimensional barb nanostructures based on the features (observed versus expected number and relative positions of peaks) of their SAXS patterns. Many feathers that lacked any higher-order scattering features besides the primary structural correlation peak ($n = 48$) or exhibited a low intensity second-order shoulder at approximately twice the dominant spatial frequency (1.879 ± 0.005; $n = 95$) were identified as the *channel*-type (figures 5*a*,*b* and 6). Both the structure factors calculated from TEM images of channel-type nanostructures [25], as well as experimental scattering data from other interconnected bicontinuous network nanostructures [33,34] support these conclusions (see §3.2). By contrast, many other feathers ($n = 75$) diagnostically exhibited two or more pronounced, higher-order peaks indicative of spherical form-factor scattering fringes [25,57] at ratios of approximately √3 (1.693 ± 0.004; $n = 75$), √7 (2.498 ± 0.010; $n = 75$) and √11 (3.475 ± 0.063; $n = 11$) and were recognized as the *sphere*-type (figures 5*c*,*d* and 6). The secondary shoulder at approximately 2^*q_{pk} in channel-type nanostructures is comparatively much broader in width and weaker in intensity relative to the primary peak than is the second-order peak (approx. $\sqrt{3}^*q_{pk}$) from sphere-type nanostructures (see electronic supplementary material, figure S2). We further corroborated many of these SAXS structural assignments of barb nanostructures based on previously published (see [3] and references therein) and our own TEM and SEM images for 39 channel- and 27 sphere-type barb

nanostructures (see electronic supplementary material, table S2).

For the remaining 40 feathers, we provisionally identified the nanostructures as the structural interpretation of their SAXS data was less straightforward and/or in some feathers, the azimuthal profiles were comparatively noisier, i.e. jagged (see figure 5 and electronic supplementary material, table S2). The azimuthal SAXS profiles of 21 such feathers ('sphere*', see electronic supplementary material, table S2) exhibited only a broad second-order peak between 1.604 and 1.737 times q_{pk}, but consistent with the distribution for unambiguous sphere-type morphologies (see electronic supplementary material, figure S2). The scattering intensities of the second-order peaks from most of these feathers were also considerably higher than the mean intensity of the channel-type second-order shoulders (see electronic supplementary material, figure S2). By contrast, the azimuthal profiles of eight feathers were noisy with only the primary scattering peak present, consistent with the channel morphology, while a further 11 feathers exhibited second-order shoulders but at smaller positional ratios (1.747–1.796) than expected ('channel*', see electronic supplementary material, table S2). These tentative nanostructural assignments were validated based on EM images (nine 'channel*' and five 'sphere*') and/or the unambiguously identified nanostructure present in other structurally coloured plumage patches on the same species or in a few cases, indirectly assumed from that in closely related taxa within the same genus (see electronic supplementary material, figure S2 and table S2). We also evaluated the relatively noisy barb morphologies present in *Myiomela leucura* (Turdidae), *Chiroxiphia caudata* (Pipridae) and *Euneornis campestris* (Thraupidae), using SEM. SEM images of *M. leucura* revealed a spindly channel morphology with anastomosing networks of β-keratin bars of variable thickness (see electronic supplementary material, figure S1*a*). SEM images of *C. caudata* and *E. campestris* revealed sphere-type nanostructures with a greater degree of polydispersity in the size and the shape of the air spheres than in typical sphere nanostructures found in their close relatives (see electronic supplementary material, figure S1*b*,*f*). These noisier nanostructures appear to be more variable (polydisperse) versions of the types of nanostructures found in their closest, structurally coloured relatives.

3.2. Structural comparisons of amorphous barb nanostructures and synthetic soft matter systems

We compared the normalized azimuthal scattering profiles of the unambiguously diagnosed instances of channel ($n = 143$) and sphere ($n = 75$) barb nanostructure to experimental light-scattering data from polymer mixtures in early and late stages of SD [33,34], and a self-assembled, amorphous film of colloidal polymer (PS) spheres, mimicking a quasi-ordered nucleation-and-growth nanostructure (figure 5*a*–*d*).

The shape of the scattering profile of a classical spinodal mixture is scale independent; the overall structure of spinodal morphologies are universal even though the specific structure in a phase-separating sample may differ locally [39,40], but experimentally, there is substantial variation between early and late stages of SD at intermediate and high q [33,34,58,59]. The experimental spinodal polymer profiles [39,40] provide a reasonable fit to the normalized channel-type scattering profiles from feather barbs at low q (figure 5*a*), even though the width (FWHM) of the primary SAXS peak of channel-type nanostructures narrows as the dominant length scale of the nanostructure increases, i.e. for those producing longer wavelength colours (figure 5*b* and electronic supplementary material, figure S3a). At high q, the polymer spinodal morphologies lack any higher-order feature at the early stage or exhibit a second-order shoulder at approximately 2 or approximately $3q_{pk}$ at the late stage [33,34]. Similarly, the channel-type barb nanostructures either lack or exhibit a shoulder or second-order maximum at approximately twice the peak spatial periodicity (mean 1.87) (figures 5*a*,*b* and 6). However, the positions of the secondary shoulder from the channel nanostructures are probably underestimated because such shallow (broad and low intensity, see electronic supplementary material, figure S2) features are difficult to precisely estimate through curve-fitting procedures.

The SAXS scattering profile from a film of self-assembled, quasi-ordered, colloidal polymer spheres reveals a series of higher-order form factor diffraction (fringes) peaks at similar relative positions ($\sqrt{3}$ and $\sqrt{7}$) to those seen in azimuthal profiles of sphere-type nanostructures (figure 5*c*,*d*). The width (FWHM) of the primary SAXS peak of sphere-type nanostructures is also in good agreement with that of the self-assembled, amorphous PS spheres. (The X-ray scattering from an array of solid spheres is indistinguishable to that from its inverse structure—air spheres in solid—and therefore this direct comparison is valid according to Babinet's theorem [31].) Although the PS spheres are self-assembled into an amorphous structure, the spheres themselves were not synthesized *in situ* by a nucleation-and-growth process; however, the scattering profile of a three-dimensional amorphous array of spheres grown by a nucleation-and-growth mechanism should be similar [57]. The number and strength (intensity and width) of the higher-order peaks in the sphere-type nanostructures are sample-specific, and reflect the degree of quasi-periodic or nearest-neighbour order and sphere size monodispersity.

3.3. Comparative structural properties of amorphous barb nanostructures

We examined the width (FWHM) of the primary SAXS peak, Δq, to quantitatively characterize the extent of spatial periodicity in the channel and sphere classes of amorphous nanostructures ($n = 255$; 'structured' and 'structured*' were excluded; see electronic supplementary material, table S2).

The spatial coherence length, ξ, is given by $2\pi/\Delta q$. For ordered systems, ξ describes the crystalline domain size, whereas in quasi-ordered or amorphous systems, the coherence length (after scaling by the corresponding peak spatial periodicity, ξ/D) can provide a measure of the extent of short-range nearest-neighbour

order [13,60]. For both classes of amorphous barb nanostructures, ξ is only a few times the dominant length-scale of spatial correlations, D ($2\pi/q_{pk}$), reflecting the very local nature of spatial order in these systems [13]. However, the mean structural FWHM (Δq) of sphere nanostructures is significantly smaller compared with channels (one-way ANOVA, $F = 26.82$, $p < 0.001$, $n = 255$), even after scaling by the corresponding peak spatial frequency of structural correlations, q_{pk} (one-way ANOVA, $F = 28.51$, $p < 0.001$, $n = 255$), suggesting that sphere-type nanostructures are more ordered, or have a larger coherence length than channel-type nanostructures (see electronic supplementary material, figure S3).

In addition, the FWHM of the primary SAXS peak increases significantly with the dominant spatial frequency of structural correlations, q_{pk}, for both channel- ($r^2 = 0.22$, $p < 0.001$) and sphere-type ($r^2 = 0.29$, $p < 0.001$) nanostructures (see electronic supplementary material, figure S3*a*,*b*). However, the statistical significance of this relationship persists only for channel-type nanostructure ($r^2 = 0.067$, $p = 0.001$), after scaling the FWHM by the corresponding q_{pk} (see electronic supplementary material, figure S3*c*,*d*). In other words, channel-type nanostructures with larger size scale of spatial periodicity (i.e. D) producing longer wavelength colours have a smaller structural (SAXS) peak width, and consequently a larger coherence length or greater short-range order. In contrast, the sphere-type nanostructures appear to be nearly scale invariant as revealed by the same relative widths of the structural peaks across all length scales (see electronic supplementary material, figure S3*d*). These structural differences between channel and sphere morphologies are perhaps a result of their dissimilar processes of phase separation and arrest during intracellular self-assembly, which are also probably affected by the subsequent desiccation of medullary barb cells in different ways.

3.4. Comparative optical function of amorphous barb nanostructures

The slaty blue-black to pale greyish-blue feathers with rudimentary ('structured' and 'structured*') barb nanostructures generally exhibited a broad, low intensity, 'sperm-whale'-shaped reflectance profile with a gradually decreasing reflectance at longer wavelengths and a more rapid decline at shorter wavelengths. The peak parameters from the optical reflectance of these feathers could not all be consistently estimated (see electronic supplementary material, table S2) and are therefore excluded from further optical analyses. Nevertheless, the SAXS results demonstrate that these feathers are sufficiently nanostructured at the appropriate length scales to produce the observed colours via constructive interference (figure 4).

The spectral peaks in the optical reflectance measurements of the structurally coloured feathers with channel- and sphere-type nanostructures characterized in this study varied from 343.83 to 639.37 nm ($n = 255$; see electronic supplementary material, table S2). Many feathers, particularly royal (medium) blue to turquoise (light) blue ones, with either class of barb nanostructure ($n = 86$), exhibited a characteristic bimodal reflectance profile with an additional peak in the ultraviolet (UV)/violet distinct from the primary reflectance peak in the visible (400–700 nm) region (figure 7*d*–*f*,*m*–*o*, and electronic supplementary material, table S2). These secondary (short wavelength) peaks are qualitatively quite different from the relatively low intensity UV pigmentary (carotenoid) transmittance peaks seen in nanostructured feather barbs with cortical pigmentation, for instance, in structural greens (figure 7*g*–*i*,*q*). The dip between the two peaks in the former are relatively shallower and the secondary peak is nearly of the same amplitude or higher than the primary single-scattering peak (figure 7). Unlike the UV peaks in spongy barb nanostructures with cortical pigments, these secondary peaks are of structural origin owing to the double scattering of light and not explained by the higher-order structural correlations in the X-ray scattering data [36,37]. Diagnostically, the double scattering peaks occur at nearly constant relative spectral ratio to one another ($1/\sqrt{2}$) as expected from optical theory [36,37] (criterion 1). Moreover, double scattering peaks are also depolarized (criterion 2) and exhibit reverse angular dispersion (see electronic supplementary material, figure S4*b*–*f*) that is specifically predicted by optical theory (criterion 3) [36,37], whereas the static spectral features that are produced by pigmentary absorption are not (see electronic supplementary material, figure S4*g*,*h*). We have described the complete mechanistic basis of the double scattering phenomenon in detail elsewhere [36,37]. We tentatively identified 58 of these 86 feathers as double scattering candidates based on criterion 1 alone (see electronic supplementary material, table S2), while we were able to unambiguously document double scattering in the remaining 28 feathers based on criterion 2 and/or 3 (see electronic supplementary material, figure S4*b*–*f*). Here, we mainly consider the primary optical reflectance peak, which originates from the single scattering of incident light whereby each incident photon is scattered only once before it exits the nanostructure [13].

Many feathers ($n = 77$) producing structural greens and longer wavelength hues with reflectance peaks above 500 nm have distinct spectral indications of the presence of carotenoid or psittacofulvin pigments in the outer β-keratin cortex of the barb, the mechanistic basis of which are well established for many species [3,14,61]. Unlike a typical sigmoidal reflectance profile of carotenoid pigmented barbs that plateau at higher wavelengths [10], the reflectance from these feathers were distinctly peaked or saturated, but with a relatively sharp cessation of the reflectance intensity on the short-wavelength side of the peak (figure 7*g*–*i*,*p*–*r* and electronic supplementary material, figure S4*g*,*h*). In addition, the reflectance spectra of these feathers showed a minor UV transmittance peak at approximately 350 nm and/or several low intensity sub-peaks at intermediate wavelengths [3,14,61]. In contrast to double scattering feathers, these pigmentary spectral features were angle-independent (see electronic supplementary material, figure S4*g*,*h*). Therefore, we conservatively excluded these nanostructures for analyses involving the saturation or widths (FWHM) of the primary reflectance peaks, as the short and middle wavelength pigmentary

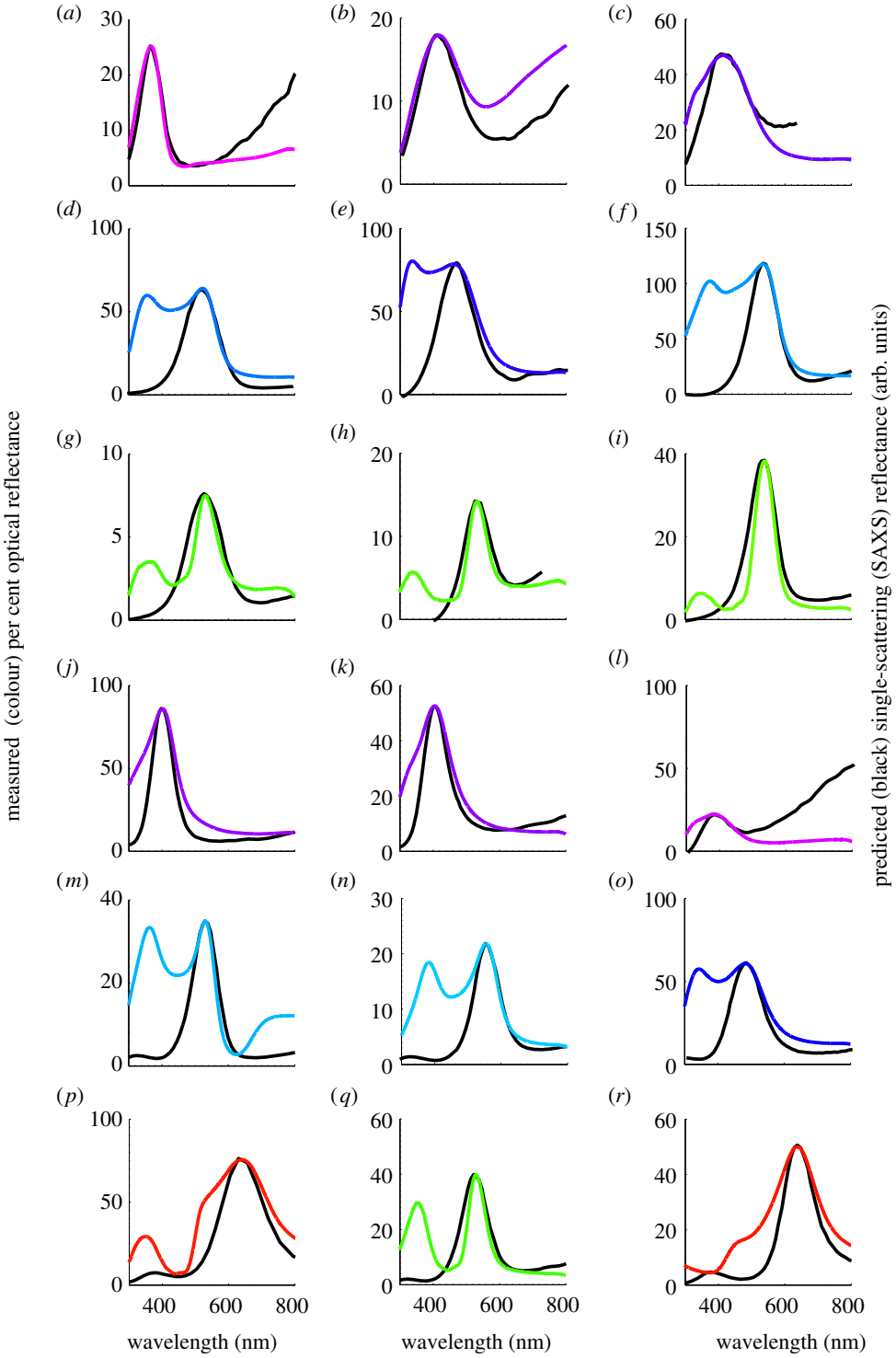

Figure 7. Single-scattering SAXS reflectance predictions for the primary optical peaks of channel (*a*–*i*) and sphere-type (*j*–*r*) amorphous barb nanostructures. SAXS single-scattering reflectance predictions (black lines) and measured normal incidence reflectance curves (coloured lines) for (*a*) UV (black) belly feather barbs of *Charmosyna papou* (Psittacidae), (*b*) violet primary feather barbs of *Acryllium vulturinum* (Psittacidae), (*c*) royal blue rump feather barbs of *S. sialis* (Turdidae), (*d*) sky blue rump feather barbs of *Alcedo atthis* (Alcedinidae), (*e*) deep azure blue back feather barbs of *Irena puella* (Irenidae), (*f*) electric blue wing covert feather barbs of *Pitta maxima* (Pittidae), (*g*) emerald green back feather barbs of *Ailuroedus buccoides* (Ptilonorhynchidae), (*h*) emerald green back feather barbs of *Charmosyna papou* (Psittacidae), (*i*) emerald green back feather barbs of *Calyptomena whitehadi* (Eurylaimidae), (*j*) deep blue throat feather barbs of *Tangara chilensis* (Thraupidae), (*k*) royal blue wing covert feather barbs of *Wetmorethraupis sterrhopteron* (Thraupidae), (*l*) violet scapular feather barbs of *Conirostrum albifrons* (Thraupidae), (*m*) dark turquoise blue back feather barbs of *C. maynana* (Cotingidae), (*n*) sky blue back feather barbs of male *Tersina viridis* (Thraupidae), (*o*) azure blue rump feather barbs of *Lepidothrix serena* (Pipridae), (*p*) golden yellow crown feather barbs of *Lepidothrix vilasboasi* (Pipridae), (*q*) electric green back feather barbs of *Chloronis riefferii* (Thraupidae), (*r*) golden crown feather barbs of *Tangara larvata* (Thraupidae). The colour of the measured reflectance curves is approximately coded to the colour of the feather barbs based on the spectral position of the primary reflectance peak.

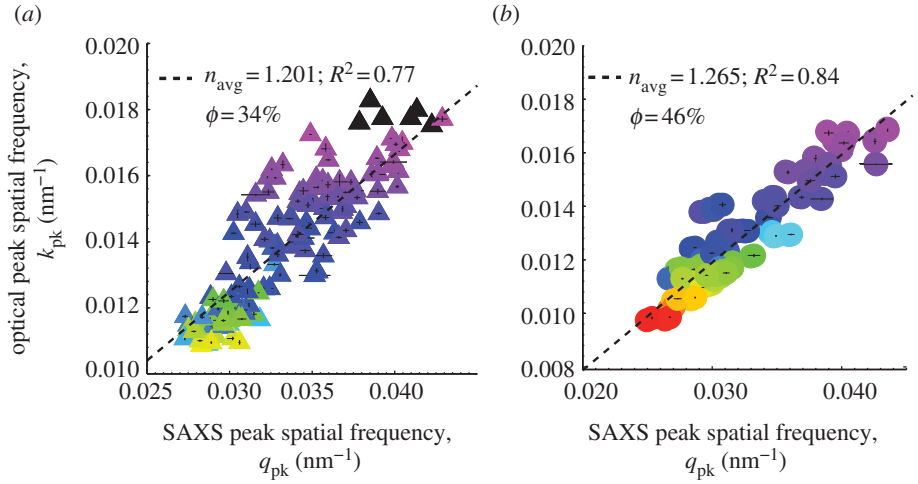

Figure 8. Regression plots of the primary optical peak hue from normal incidence reflectance measurements expressed as peak spatial frequency ($k_{pk} = 2\pi/\lambda_{pk}$) against the dominant spatial frequency of structural correlations (q_{pk}) measured using SAXS for (*a*) channel- (shaded triangles) and (*b*) sphere-type (shaded circles) nanostructures. For both nanostructural classes, the size of the nanostructural periodicity measured by SAXS strongly predicts, i.e. scales with the measured primary peak hue, demonstrating that the underlying barb nanostructures are tuned to produce the observed structural colours. The inverse of twice the slope of the regression yields n_{avg}, the average or effective refractive index (and hence ϕ, the keratin volume fraction) for each class of nanostructure. The estimated n_{avg} and ϕ for sphere nanostructures on the whole (1.265, 46%) is significantly higher than that for channel morphologies (1.201, 34%) and congruent with predictions of the phase separation hypothesis. The colour of each triangle or circle is coded to the approximate colour of the corresponding feather (UV colours in black). The vertical and horizontal lines at each data point indicate the standard error of the mean (s.e.m).

absorption could lead to an underestimation of their actual widths (see figure 7*g–i*,*p–r* and electronic supplementary material, figure S4*g*,*h*). However, the spectral position of the reflectance peak or hue (λ_{pk}) is relatively unaffected by the pigmentary absorption and the inclusion or exclusion of these data here did not significantly alter the results.

3.4.1. Single-scattering optical predictions of amorphous barb nanostructures

Based on single scattering theory, we applied Bragg's Law (equation (2.1)) to the azimuthal SAXS profiles to obtain the single scattering optical reflectance predictions of amorphous barb nanostructures [38,50]. From equation (2.1), for a given nanostructure, the predicted peak hue depends on the size of the nanostructure measured by SAXS (D) and the average or effective refractive index of the nanostructure (n_{avg}), while the predicted optical saturation or peak width depends on the spatial coherence length, ξ ($2\pi/\Delta q$) alone. Although we predicted the optical reflectance curves for all 255 barb nanostructures, here we present these results only for a small subset of feathers, owing to space limitations (figure 7). We summarize below the goodness of fit of SAXS single scattering optical predictions to normal-incidence reflectance measurements, based on pairwise regressions of peak hue and saturation of the reflectance measurements and reflectance predictions for both channel- and sphere-type nanostructures.

There is a strong positive correlation between the measured primary optical peak hue (expressed in spatial frequency, $k = 2\pi/\lambda_{pk}$) and the dominant spatial frequency of structural correlations, i.e. the primary SAXS peak wavevector (q_{pk}) for both channel and sphere-type nanostructures (figure 8*a*,*b*). For both classes of barb nanostructure, the size of the nanostructural periodicity scales strongly with primary peak hue, demonstrating that the underlying barb nanostructures are tuned to produce the observed structural colours. The correlation is stronger for sphere-type ($r^2 = 0.84$) than for channel-type nanostructures ($r^2 = 0.77$). This relationship persists even for those barb nanostructures producing longer wavelength colours (peaking at approx. 550 nm and higher) that probably involve cortical pigments.

Although the average inter-scatterer spacing D or the dominant length scale of nanostructural periodicity can be directly measured using SAXS, there is no direct method to measure the average or effective refractive index of the amorphous barb nanostructure, n_{avg}. We used two independent methods to estimate n_{avg}: (i) by correlating normal incidence optical measurements with SAXS structural data using equation (2.1) and (ii) from angle-resolved optical reflectance measurements.

First, we use the regression relationship in figure 8 to estimate the average or effective refractive index (n_{avg}), and hence the filling or volume fraction (ϕ) of β-keratin for each class of nanostructure as a whole, using the Maxwell–Garnett effective medium approximation [51]. The inverse of twice the slope of the regression yields n_{avg} (see equation (2.1)). The estimated global n_{avg} for sphere nanostructures (1.265; 46% ϕ) is significantly larger than that for channel morphologies (1.201; 34% ϕ; one-way ANOVA, $F = 31.45$, $p < 0.001$, $n = 255$). This result is congruent with predictions of the phase separation hypothesis, since, under similar thermodynamic conditions ($k_B T/\chi$), nucleation-and-growth should occur at higher volume fractions of keratin (hence n_{avg})

compared with SD [25,38]. Further, for each of the 255 barb nanostructures, we calculated its n_{avg} by substituting the values of q_{pk} from SAXS profiles and λ_{pk} from normal-incidence optical reflectance data in equation (2.1) (see electronic supplementary material, table S2). The n_{avg} estimated thus is significantly positively correlated with the peak optical hue, λ_{pk} for both channels ($r^2 = 0.44$, $p < 0.001$) and spheres ($r^2 = 0.17$, $p < 0.001$) (see electronic supplementary material, figure S5*a*,*b*). The increase in n_{avg} with λ_{pk} suggests that production of a longer wavelength hue by either class of nanostructure involves increases in both the length scale of spatial periodicity (D) (figure 8) as well as the keratin volume fraction (n_{avg}), instead of independently varying one parameter or the other. The scatter in the plot probably reflects variation in the length scale of spatial periodicity and keratin volume fraction (hence n_{avg}) among different species with similar structurally coloured plumages.

Since amorphous feather barb nanostructures have the same angular dispersion for specular reflection and diffuse scattering peaks, they both share a common physical origin, and under directional lighting conditions, the reflectance peak depends only on the angle between incidence and observation [13,36,37]. Exploiting this, we measured the angle-resolved diffuse scattering spectra of barb nanostructures for a small subset of channel- ($n = 11$) and sphere-type ($n = 11$) nanostructures. We estimated n_{avg} independent of the SAXS data by analysing the angular dispersion of the primary optical peak using a modified form of Bragg's Law (equation (2.1)), taking into account the reduced angle with respect to the normal at which light travels inside the barb nanostructure (i.e. Snell's Law):

$$\lambda_{pk}(\theta) \;=\; 2D(n_{avg}^2 - \sin^2\theta)^{1/2}, \qquad (3.2)$$

where the primary optical peak position, λ_{pk}, varies with θ, the angle between incidence and observation. A plot of λ_{pk}^2 against $\sin^2\theta$ yields n_{avg} ($\sqrt{y}$-intercept) but also D ($0.5/\sqrt{\text{slope}}$) [62,63] (see electronic supplementary material, figure S6*a*). The corresponding values of D (see electronic supplementary material, figure S6*b*) and n_{avg} (see electronic supplementary material, figure S6*c*) obtained from these two independent methods are consistent and agree to be within 7 per cent of each other. Unlike photonic crystals, however, the optical diffuse scattering and specular reflection intensities of amorphous barb nanostructures falls off rapidly at shallower angles [13] and so the SAXS and normal incidence optical characterization (method 1) of the amorphous barb photonic nanostructures is probably more accurate.

We obtained measured and predicted optical bandwidths for both channel- and sphere-type nanostructures by scaling the saturation (FWHM) of the measured reflectance and the width (FWHM) of the corresponding single scattering azimuthal SAXS profiles by the respective peak hue (λ_{pk}) and peak spatial frequency (q_{pk}), in order to compare across feathers of different colours and nanostructural length scales (feathers with cortical pigments were excluded because pigmentary absorption can lead to an underestimation of the true peak widths). The bandwidth of the primary optical peak is positively correlated with the scaled widths of the primary SAXS peak for both channel ($r^2 = 0.47$) and sphere-type ($r^2 = 0.71$) nanostructures (see electronic supplementary material, figure S7*a*,*b*). This result indicates that the width of the primary single scattering SAXS peak reasonably predicts the optical saturation of the nanostructure. Concordant with the structural results (see §3.3), nanostructures with larger size scales of spatial periodicity (i.e. D) generally make more saturated colours (smaller FWHM). Variations in the inter-scatterer spacing, D (which increase the SAXS peak width thereby decreasing the coherence length, ξ), result in broader, less saturated structural colours. The measured optical bandwidth is consistently larger than the single-scattering structural prediction for both nanostructural classes (see electronic supplementary material, figure S7*a*,*b*), probably because of multiple scattering [36].

4. DISCUSSION

We have characterized the nanostructure and optical properties of hundreds of structurally coloured feathers encompassing the gamut of non-iridescent structural hues from diverse taxa across the phylogeny of birds using a combination of SAXS, electron microscopy, normal incidence and angle resolved spectrophotometry. The SAXS structural information enabled quantitative diagnoses of the channel and sphere-type nanostructures, and documented the presence of a predominant, isotropic, short-ranged order. The nanostructural variation in refractive index is of the appropriate length scales to produce strong reinforcement of a narrow band of scattered wavelengths. Noisy and ambiguous cases of structural diagnoses from SAXS data were corroborated by EM data. Additionally, we have identified a previously unknown class of slaty blue-black to blue-grey structural colours that are produced by rudimentary or highly variable versions of channel- and sphere-type nanostructures. Overall, the SAXS results represent a substantial improvement over Fourier analyses of EM [3,7–9,17–19] and three-dimensional electron tomography data [26].

SAXS structural data also provided good predictions of the primary, single-scattering peaks in optical reflectance measurements. Both the spectral position and shape (FWHM) of the peaks in the azimuthal SAXS profiles were highly correlated with those of the corresponding primary peak of optical reflectance measurements (figure 8 and electronic supplementary material, figure S7). The discrepancies between the optical measurements and structural predictions especially for short wavelength peaks ($\lambda_{pk} < 450$ nm; electronic supplementary material, figure S7) barbs can be explained in part by the multiple scattering of light, since scattering (and multiple scattering) is stronger at shorter wavelengths of light, which could result in significant broadening of the optical reflectance peaks.

We have also documented quantitative differences in the nature of structural colour production by sphere- and channel-type nanostructures. On average, the colours generated by sphere-type nanostructures are significantly more saturated (smaller FWHM) than those produced by

channel-type, and this has a strong nanostructural basis (see electronic supplementary material, figure S3). However, the FWHM of the primary optical peaks produced by both types of nanostructures decreases (i.e. saturation increases) with increasing peak hue (i.e. longer wavelength colours), reflecting the underlying increase in short-range quasi-periodic order within the nanostructure with increasing nanostructural size (see electronic supplementary material, figures S3 and S7).

4.1. Development of amorphous feather barb nanostructures

The development of the channel-type amorphous feather barb nanostructure in Blue-and-Yellow Macaw proceeds in the spongy medullary cells in the telling absence of any precursor biological template or pre-pattern created by cytoskeleton, organelles or membranes [25]. During feather cell maturation, capillary forces owing to the drying of the spongy cells apparently drive higher molecular weight materials to the cell's periphery, resulting in dense peripheral aggregations of granular materials and a large, electron-lucid cytoplasmic volume in the centre of the cell. The channel-type nanostructure arises spontaneously from within the peripheral regions of dense, granular cytoplasmic material, coarsens over time and grows to fill the volume of the cell [25]. We have hypothesized that this self-assembly process occurs by phase separation, possibly regulated by the rates of β-keratin expression and polymerization [25,38]. How could phase separation stop at the correct size to be able to produce the appropriate colour? Phase separation could be arrested by either mechanical jamming or a glass-transition in the β-keratin protein phase [25,38], thus determining the characteristic length scale of the nanostructure. Phase separation has been studied in detail in other protein solutions such as lysozyme, etc. [45,64]. These hypotheses are ultimately testable with experimental analyses of the self-assembly of β-keratin polymers. Upon barb cell death, the cytoplasm dries out completely, and is replaced by air resulting in the final keratin-and-air amorphous photonic nanostructure.

The morphological similarities in the previously published EM images [3,25] and experimental X-ray scattering data reported here (figure 5*a–d*) for channel- and sphere-type amorphous barb nanostructures and synthetic self-assembled soft matter systems is congruent with the hypothesis that avian barb nanostructures probably self-assemble via arrested phase separation of polymerizing β-keratin from the cellular cytoplasm, as suggested earlier for a few avian species [25,38]. Although the channel- and sphere-type barb nanostructures, respectively, appear to be similar to morphologies observed during classical phase separation via SD and nucleation-and-growth, to conclude that they indeed develop via phase separation, let alone assign a particular mode of phase separation using just morphology is not straightforward [45–47]. The lack of a perfect agreement between channel-type barb nanostructures and classical spinodal morphologies perhaps suggests that there may be important differences between a biological soft matter system and a simple binary fluid de-mixing, perhaps involving some viscoelastic phase separation processes [45–47]. Nevertheless, careful observations of β-keratin self-assembly in developing feathers, together with *in vitro* investigations are necessary to pinpoint the precise mechanisms of their self-assembly.

4.2. Double scattering of light by amorphous feather barb nanostructures

The phenomena of double scattering and cortically pigmentation of spongy nanostructures are distinguishable by their starkly differing angular dispersion (see electronic supplementary material, figure S4*b–h*), predictable spectral position of the relatively strong double-scattering peak in relation to the primary peak, polarization dependence [36,37], and by the limited classes of available pigments in birds [10]. We have documented the widespread occurrence of double scattering in the optical function of amorphous feather barb nanostructures (figure 7*d–f*,*m–o* and electronic supplementary material, table S2). Many such hues such as turquoise (light) blue (e.g. in male *Cotinga* spp., figure 7*m* and male *Tersina viridis*) include two strong and distinct spectral peaks, one in the UV (visible to birds but not to humans) and the other in green. To birds, these hues are distinct colours stimulating non-adjacent cone types (i.e. UV and medium-wavelength spectral sensitivities) in the avian retina that will be perceived by birds as distinct colours [65,66]. Thus, the double scattering spectral features probably contribute significantly to the colours of non-iridescent structural plumages perceived by birds, given that most birds can see in the UV/deep violet [11,67,68]. This suggests that the double scattering from amorphous barb nanostructures constitutes a source of rich UV signals in birds [69].

The occurrence of double scattering in the optical reflectances of amorphous barb nanostructures is probably underestimated here, since at shorter wavelengths, it is much harder to separately estimate the double scattering peak from the primary peak and the sensitivity of the spectrophotometer steeply decreases. In fact, many reflectance profiles with a short-wavelength primary peak but without an obvious double-scattering peak have a distinct shoulder on the short-wavelength side of the reflectance spectrum (e.g. many *Malurus* spp. and tanagers, see figure 7*j*,*k*).

4.3. Structure–pigment interactions

The combination of spongy medullary barb photonic nanostructure and carotenoid or psittacofulvin pigments is well known to produce longer wavelength colours that cannot be produced by pigments alone, such as structural greens [3,14,61]. Structural analyses of these feather barbs demonstrate that the underlying barb nanostructures are larger in spatial periodicity than those producing purely structural hues (such as UV, violet and blue). Indeed, the underlying spongy medullary keratin nanostructure in each case was tuned to the appropriate length scale to produce the observed reflectance peak by constructive interference

alone (figure 8 and electronic supplementary material, table S2). Therefore, contrary to prevalent simplistic notions of colour mixing (structural blue + pigmentary yellow = green) [70], the peaked or saturated green colours in feather barbs are produced by a combination of medullary barb nanostructures tuned to produce those longer wavelength colours and the absorption of some portions of the shorter wavelength double-scattering peak and the intermediate wavelengths between the two peaks. Similar structure–pigment interactions have been proposed in saturated yellow (*Ramphastos toco*, Ramphastidae) and orange (*Tragopan caboti*, Phasianidae) colours in avian skin [3,71].

In feathers with structure–pigment interactions, the incident light first passes through the pigmented outer cortex layer of the barbs, a portion of which is absorbed by the pigments, and the rest is transmitted to the underlying medullary layer of nanostructure. The pigment acts like a band-pass filter, i.e. only the range of wavelengths that is selectively transmitted by the pigments in the cortex can be scattered by the nanostructure underneath. However, the nanostructure is tuned to constructively reinforce and scatter only a portion of the transmitted pigmentary reflectance, with the longer wavelengths getting destructively interfered and thereby reducing the typical broadband longer wavelength reflectance of the pigments, just like in avian skin [3,71]. The light scattered by the nanostructure once again passes through the pigmented cortex on its way out of the feather barb. The result is a uniquely saturated, brighter longer wavelength colour that is spectrally quite distinct from both the superficial pigments and the nanostructure below (figure 7). Furthermore, just as in avian skin [71], there appears to be no intrinsic constraints to the production of longer-wavelength structural colours in feather barbs by constructive interference from amorphous nanostructures (figure 8). However, given the propensity for double scattering owing to the amorphous nature of spongy barb nanostructures [36,37] (figure 7*d–f*,*m–o* and electronic supplementary material, table S2), pure (highly saturated) non-iridescent long-wavelength structural hues are unlikely to occur in feather barbs [72].

The deposition of spectrally absorbing pigments superficially in the barb cortex can result in the attenuation of the double scattering short-wavelength structural peak in the optical reflectance (see above), resulting in more saturated long-wavelength hues (e.g. purer structural greens and yellows as in many tanager feathers). However, a portion of the short-wavelength double-scattering peak can be reinforced, if the transmission spectra of the deposited pigments have an overlapping but relatively less intense UV peak (characteristic of carotenoids like lutein, for instance; figure 7*g–i*,*p*,*q*) or not (as in the case of many tanagers; figure 7*r*). In bird species with both non-iridescent blue and structural green plumage patches, the respective absence or presence of cortical pigments in the barb appears to be the general mechanism by which plumage reflectance differences arise between blue and green patches of sexually monomorphic species (e.g. *Corythaeola cristata*, Musophagidae; *Merops viridis*, Meropidae; *Eumomota superciliaris*, Momotidae; *Aulacorynchus prasinus*, Ramphastidae; *Forpus xanthopterygius*, Psittacidae; *Calyptomena hosii*, Eurylaimidae; *Vireolanius pulchellus*, Vireonidae; *Erythrura trichroa*, Estrildidae; *Chlorophonia occipitalis*, Fringillidae; *Tangara chilensis*, Thraupidae; see electronic supplementary material, table S2), and between homologous blue (usually in males) and green (usually in females) patches in the opposite sexes of sexually dichromatic species (e.g. *Lepidothrix* spp., Pipridae; *Cyanerpes cyaneus*, *Te. viridis*, Thraupidae; see electronic supplementary material, table S2).

In the optical reflectance of a further 21 (out of 255) feather barbs examined (see electronic supplementary material, table S2), a longer wavelength pigmentary reflectance plateau from apparently modified keto-carotenoids [73] or phaeo-melanins complements a shorter wavelength (violet to blue) single or double structural peaks, producing distinct extra-spectral colours including vivid shades of violets and purples to blue hues with hints of lilac (e.g. *Acryllium vulturinum*, Numididae, figure 7*b*; *C. maynana*, figure 7*m*; *Malurus coronatus*, Maluridae; *Sitta oenochlamys*, Sittidae). Thus, complex interactions between structural and pigmentary mechanisms produces hues that are unavailable to either modes of colour production, but additional research is required to understand the nature of these interactions more precisely.

4.4. Evolution of non-iridescent barb structural colours

Non-iridescent, structural colour-producing three-dimensional amorphous barb nanostructures appear to have independently evolved at least 44 times within 41 families across Aves, conservatively assuming a single evolutionary origin within each family examined, with an additional five families possessing species with marginal barb structural coloration (see electronic supplementary material, table S2). However, there appears to be multiple origins of non-iridescent barb structural colour within some families (see electronic supplementary material, table S2). An accurate estimate of the number of evolutionary gains and losses of barb structural colours in extant birds requires a well-resolved phylogeny of all birds. Therefore, a formal, detailed macro-evolutionary analysis of barb structural colours will have to await significant progress in unravelling the evolutionary tree of birds. Nevertheless, the phylogenetic distribution of photonic barb nanostructures at the inter-ordinal level is distinctly non-random. The channel nanostructures ($n = 36$) occur more frequently than the spheres ($n = 8$) among both passerine (perching) and non-passerine birds (electronic supplementary material, table S2). For each avian family with barb structural colours, we have examined multiple species in different genera and multiple plumage patches within at least one species. In nearly every instance, all specimens sampled within a family shared the same class of nanostructure. However, we identified a few instances in which the nanostructures varied within a single avian family. Within the tanagers (Thraupidae), *Cyanicterus cyanicterus*, *Diglossa cyanus* (see electronic supplementary material, figure S1*e*) and *Xenodacnis petersi* possess channel-type nanostructure while the rest of the tanagers examined have spheres.

But these three species are closely related members of a distinct branch of the family [74], and this could represent a genuinely independent evolutionary origin of colour-producing nanostructure within the family. Similarly within the cardinals and grosbeaks (Cardinalidae), all taxa examined appear to possess a channel-type nanostructure except *Cyanoloxia glaucocaerulea*, which has the sphere-type morphology, based on SAXS data and SEM images (see electronic supplementary material, figure S1*g*,*h*).

4.5. Biomimicry lessons for amorphous photonics

Recently, there has been a flurry of interest in the optical properties, design and synthesis of amorphous nanostructures at optical length scales, as they possess both isotropic optical properties (non-iridescence) and omnidirectional photonic bandgaps at high refractive index contrast [75–80], unlike conventional, angle-dependent photonic crystals [6]. In contrast to amorphous 'opal' nanostructures of synthesized dielectric spheres featured in contemporary engineering approaches [75,78–80], the spongy feather barbs possess an amorphous 'inverse-opal' nanostructure, which is likely to possess better optical properties than their 'opal' counterparts, by analogy to photonic crystals [6]. Indeed, the optical properties of feather barbs currently surpass those of engineered amorphous colloidal photonic materials [51]. Amorphous photonic nanostructures that are probably self-assembled in bird feather barbs with pronounced isotropic short-range order could therefore provide a useful, tunable biotemplate for positive cast replication or dielectric infiltration. A thorough understanding of the physics and development of organismal structural colour that have evolved over millions of years of selection for a consistent optical function may thus guide bio-inspired technological innovations [5,51,81–83].

This work was supported with seed funding from the Yale NSF-MRSEC (DMR 1119826) and NSF grants to R.O.P. (DBI-DBI-0078376), H.C. (PHY-0957680) and E.R.D. (CAREER CBET-0547294) as well as Yale University funds to V.S. and R.O.P. R.O.P. would like to acknowledge support of the Ikerbasque Science Fellowship and the Donostia International Physics Center. We thank two anonymous reviewers for their helpful comments, Thomas Valqui for his kind permission to use his photograph of *C. maynana* and Kristof Zyskowski for help with bird taxonomy. We are grateful to the Yale Peabody Museum of Natural History, the University of Kansas Natural History Museum and Biodiversity Research Center, the American Museum of Natural History (Paul Sweet), the Natural History Museum at the Academy of Natural Sciences (Nate Rice), the Harvard University Museum of Comparative Zoology (Jeremiah Trimble and Scott Edwards), and the University of Oxford Natural History Museum (Malgosia Nowak-Kemp) for the feather samples. Tim Quinn obtained TEM images of some bird feather barbs. SAXS data on bird feathers were collected with the help of Alec Sandy and Suresh Narayanan at beam line 8-ID-I of the Advanced Photon Source at Argonne National Labs, and supported by the US Department of Energy, Office of Science, Office of Basic Energy Sciences, under Contract No. DE-AC02-06CH11357. We thank Nick Terrill and Tobias Richter for help with SAXS data collection at beamline I22 of the Diamond Light Source (sm6905-1) that contributed to some of the results presented here. V.S. initiated, designed and performed the research with R.O.P.; J.D.F. prepared the biomimetic bidisperse PS sphere films; H.N. and S.-F.L. collected angle-resolved data on a few feathers; V.S. analysed and discussed the data with all authors; and V.S. wrote the manuscript with E.R.D and R.O.P.

REFERENCES

1 Kinoshita, S., Yoshioka, S. & Miyazaki, J. 2008 Physics of structural colors. *Rep. Prog. Phys.* **71**, 076401. (doi:10.1088/0034-4885/71/7/076401)
2 Parker, A. R. 2000 515 million years of structural colour. *J. Opt. A Pure Appl. Opt.* **2**, R15–R28. (doi:10.1088/1464-4258/2/6/201)
3 Prum, R. O. 2006 Anatomy, physics, and evolution of avian structural colors. In *Bird coloration, volume 1 mechanisms and measurements* (eds G. E. Hill & K. J. McGraw), pp. 295–353. Cambridge, MA: Harvard University Press.
4 Srinivasarao, M. 1999 Nano-optics in the biological world: beetles, butterflies, birds, and moths. *Chem. Rev.* **99**, 1935–1961. (doi:10.1021/cr970080y)
5 Vukusic, P. & Sambles, J. R. 2003 Photonic structures in biology. *Nature* **424**, 852–855. (doi:10.1038/nature01941)
6 Joannopoulos, J. D., Johnson, S. G., Winn, J. N. & Meade, R. D. 2008 *Photonic crystals: molding the flow of light*, 2nd edn. Princeton, NJ: Princeton University Press.
7 Prum, R. O., Andersson, S. & Torres, R. H. 2003 Coherent scattering of ultraviolet light by avian feather barbs. *Auk* **120**, 163–170. (doi:10.1642/0004-8038(2003)120[0163:CSOULB]2.0.CO;2)
8 Prum, R. O., Torres, R. H., Williamson, S. & Dyck, J. 1998 Coherent light scattering by blue feather barbs. *Nature* **396**, 28–29. (doi:10.1038/23838)
9 Prum, R. O., Torres, R. H., Williamson, S. & Dyck, J. 1999 Two-dimensional Fourier analysis of the spongy medullary keratin of structurally coloured feather barbs. *Proc. R. Soc. Lond. B* **266**, 13–22. (doi:10.1098/rspb.1999.0598)
10 Hill, G. E. & McGraw, K. J. 2006 *Bird coloration, volume 1—mechanisms and measurements*. Cambridge, MA: Harvard University Press.
11 Hill, G. E. & McGraw, K. J. 2006 *Bird coloration, volume 2—function and evolution*, p. 528. Cambridge, MA: Harvard University Press.
12 Brink, D. J. & van der Berg, N. G. 2004 Structural colours from the feathers of the bird *Bostrychia hagedash*. *J. Phys. D Appl. Phys.* **37**, 813–818. (doi:10.1088/0022-3727/37/5/025)
13 Noh, H., Liew, S. F., Saranathan, V., Mochrie, S. G. J., Prum, R. O., Dufresne, E. R. & Cao, H. 2010 How noniridescent colors are generated by quasi-ordered structures of bird feathers. *Adv. Mater.* **22**, 2871–2880. (doi:10.1002/adma.200903699)
14 Dyck, J. 1978 Olive green feathers: Reflection of light from the rami and their structure. *Anser. Suppl.* **3**, 57–75.
15 D'Alba, L., Saranathan, V., Clarke, J. A., Vinther, J. A., Prum, R. O. & Shawkey, M. D. 2011 Colour-producing β-keratin nanofibres in blue penguin (Eudyptula minor) feathers. *Biol. Lett.* **7**, 543–546. (doi:10.1098/rsbl.2010.1163)
16 Prum, R. O. & Torres, R. H. 2003 A Fourier tool for the analysis of coherent light scattering by bio-optical nanostructures. *Integr. Comp. Biol.* **43**, 591–602. (doi:10.1093/icb/43.4.591)

17 Shawkey, M. D., Balenger, S. L., Hill, G. E., Johnson, L. S., Keyser, A. J. & Siefferman, L. 2006 Mechanisms of evolutionary change in structural plumage coloration among bluebirds (*Sialia* spp.). *J. R. Soc. Interface* **3**, 527–532. (doi:10.1098/rsif.2006.0111)

18 Shawkey, M. D., Estes, A. M., Siefferman, L. & Hill, G. E. 2005 The anatomical basis of sexual dichromatism in non-iridescent, ultraviolet-blue structural coloration of feathers. *Biol. J. Linnean Soc.* **84**, 259–271. (doi:10.1111/j.1095-8312.2005.00428.x)

19 Shawkey, M. D., Estes, A. M., Siefferman, L. M. & Hill, G. E. 2003 Nanostructure predicts intraspecific variation in ultraviolet-blue plumage colours. *Proc. R. Soc. Lond. B* **270**, 1455–1460. (doi:10.1098/rspb.2003.2390)

20 Osorio, D. & Ham, A. D. 2002 Spectral reflectance and directional properties of structural coloration in bird plumage. *J. Exp. Biol.* **205**, 2017–2027.

21 Dyck, J. 1987 Structure and light reflection of green feathers of fruit doves (*Ptilinopus* spp.) and an imperial pigeon (*Ducula concinna*). *Biologische Skrifter* **30**, 2–43.

22 Dyck, J. 1971 Structure and colour-production of the blue barbs of *Agapornis roseicollis* and *Cotinga maynana*. *Zeitschrift Zellforsch* **115**, 17–29. (doi:10.1007/BF00330211)

23 Andersson, S. 1999 Morphology of UV reflectance in a whistling-thrush: implications for the study of structural colour signalling in birds. *J. Avian Biol.* **30**, 193–204. (doi:10.2307/3677129)

24 Finger, E. 1995 Visible and UV coloration in birds: MIE scattering as the basis of color in many bird feathers. *Naturwissenschaften* **82**, 570–573. (doi:10.1007/BF01140249)

25 Prum, R. O., Dufresne, E. R., Quinn, T. & Waters, K. 2009 Development of colour-producing β-keratin nanostructures in avian feather barbs. *J. R. Soc. Interface* **6**(Suppl. 2), S253–S265. (doi:10.1098/rsif.2008.0466.focus)

26 Shawkey, M. D., Saranathan, V., Pálsdóttir, H., Crum, J., Ellisman, M. H., Auer, M. & Prum, R. O. 2009 Electron tomography, three-dimensional Fourier analysis and colour prediction of a three-dimensional amorphous biophotonic nanostructure. *J. R. Soc. Interface* **6**(Suppl. 2), S213–S220. (doi:10.1098/rsif.2008.0374.focus)

27 Argyros, A., Large, M. C. J., McKenzie, D. R., Cox, G. C. & Dwarte, D. M. 2002 Electron tomography and computer visualization of a three-dimensional 'photonic' crystal in a butterfly wing-scale. *Micron* **33**, 483–487. (doi:10.1016/S0968-4328(01)00044-0)

28 Jones, R. A. L. 2002 *Soft condensed matter*, x, 195pp. Oxford, UK: Oxford University Press.

29 Svergun, D. I., Feigin, L. A. & Taylor, G. W. 1987 *Structure analysis by small-angle X-ray and neutron scattering*, vol. xiii, 335 pp. New York, NY: Plenum Press.

30 Narayanan, T. 2009 High brilliance small-angle X-ray scattering applied to soft matter. *Curr. Opin. Colloid Interface Sci.* **14**, 409–415. (doi:10.1016/J.Cocis.2009.05.005)

31 Glatter, O. & Kratky, O. 1983 *Small angle X-ray scattering*, 2nd edn. London, UK: Academic Press.

32 Gaskill, J. D. 1978 *Linear systems, Fourier transforms, and optics*, vol. xiv, 554 pp. New York, NY: Wiley.

33 Takenaka, M. & Hashimoto, T. 1992 Scattering studies of self-assembling processes of polymer blends in spinodal decomposition 0.2. Temperature-dependence. *J. Chem. Phys.* **96**, 6177–6190. (doi:10.1063/1.462635)

34 Hayashi, M., Jinnai, H. & Hashimoto, T. 2000 Two-step phase separation of a polymer mixture. II. Time evolution of structure factor. *J. Chem. Phys* **112**, 6897–6909. (doi:10.1063/1.481321)

35 Vos, W. L., Megens, M., Kats, C. M. & Bo, P. 1997 X-ray diffraction of photonic colloidal single crystals. *Langmuir* **7463**, 6004–6008. (doi:10.1021/la970423n)

36 Noh, H., Liew, S. F., Saranathan, V., Prum, R. O., Mochrie, S. G. J., Dufresne, E. R. & Cao, H. 2010 Double scattering of light from biophotonic nanostructures with short-range order. *Opt. Exp.* **18**, 11 942–11 948.

37 Noh, H., Liew, S. F., Saranathan, V., Prum, R. O., Mochrie, S. G. J., Dufresne, E. R. & Cao, H. 2010 Contribution of double scattering to structural coloration in quasiordered nanostructures of bird feathers. *Phys. Rev. E* **81**, 051923. (doi:10.1103/Physreve.81.051923)

38 Dufresne, E. R., Noh, H., Saranathan, V., Mochrie, S. & Prum, R. O. 2009 Self-assembly of amorphous biophotonic nanostructures by phase separation. *Soft Matter* **5**, 1792–1795. (doi:10.1039/b902775k)

39 Cahn, J. W. & Hilliard, J. E. 1958 Free energy of a nonuniform system. I. Interfacial free energy. *J. Chem. Phys.* **28**, 258–267. (doi:10.1063/1.1744102)

40 Cahn, J. W. 1962 On spinodal decomposition in cubic crystals. *Acta Metallurgica* **10**, 179–183. (doi:10.1016/0001-6160(62)90114-1)

41 Lifshitz, I. M. & Slyozov, V. V. 1961 The kinetics of precipitation from supersaturated solid solutions. *J. Phys. Chem. Solids* **19**, 35–50. (doi:10.1016/0022-3697(61)90054-3)

42 Wagner, C. 1961 Theorie der alterung von niederschlagen durch umlosen (Ostwald-Reifung). *Z. Elektrochem.* **65**, 581–591.

43 Viswanatha, R. & Sarma, D. D. 2007 Growth of nanocrystals in solution. In *Nanomaterials chemistry* (eds C. N. R. Rao & A. Müller & A. K. Cheethan). Weinheim, Germany: Wiley.

44 Beattie, J. K. 1989 Monodisperse colloids of transition-metal and lanthanide compounds. *Pure Appl. Chem.* **61**, 937–941. (doi:10.1351/pac198961050937)

45 Tanaka, H. 2000 Viscoelastic phase separation. *J. Phys.-Condens. Matter* **12**, R207–R264. (doi:10.1088/0953-8984/12/15/201)

46 Tanaka, H. & Nishikawa, Y. 2005 Viscoelastic phase separation of protein solutions. *Phys. Rev. Lett.* **95**. (doi:10.1103/Physrevlett.95.078103)

47 Tanaka, H. 1996 Universality of viscoelastic phase separation in dynamically asymmetric fluid mixtures. *Phys. Rev. Lett.* **76**, 787–790. (doi:10.1103/PhysRevLett.76.787)

48 Benedek, G. B. 1971 Theory of transparency of the eye. *Appl. Opt.* **10**, 459–473. (doi:10.1364/AO.10.000459)

49 Auber, L. 1957 The structures producing 'non-iridescent' blue color in bird-feathers. *Proc. Zool. Soc. Lond.* **129**, 455–486. (doi:10.1111/j.1096-3642.1957.tb00307.x)

50 Saranathan, V., Osuji, C. O., Mochrie, S. G., Noh, H., Narayanan, S., Sandy, A., Dufresne, E. R. & Prum, R. O. 2010 Structure, function, and self-assembly of single network gyroid (I4132) photonic crystals in butterfly wing scales. *Proc. Natl Acad. Sci. USA* **107**, 11 676–11 681. (doi:10.1073/pnas.0909616107).

51 Forster, J. D. *et al.* 2010 Biomimetic isotropic nanostructures for structural coloration. *Adv. Mater.* **22**, 2939–2944. (doi:10.1002/adma.200903693)

52 Wojdyr, M. 2010 Fityk: a general-purpose peak fitting program. *J. Appl. Crystallogr.* **43**, 1126–1128. (doi:10.1107/S0021889810030499)

53 Giacovazzo, C. 2002 *Fundamentals of crystallography*, vol. xix, 825 pp. Oxford, New York: Oxford University Press.

54 Förster, S., Timmann, A., Konrad, M., Schellbach, C., Meyer, A., Funari, S. S., Mulvaney, P. & Knott, R. 2005 Scattering curves of ordered mesoscopic materials. *J. Phys. Chem. B* **109**, 1347–1360. (doi:10.1021/jp0467494)

55 Oppenheim, A. V., Willsky, A. S. & Nawab, S. H. 1997 *Signals and systems*, 2nd edn., vol. xxx, 957 pp. Upper Saddle River, NJ: Prentice-Hall.

56 Neter, J., Wasserman, W. & Kutner, M. H. 1990 *Applied linear statistical models: regression, analysis of variance, and experimental designs*, 3rd edn., vol. xvi, 1181pp. Homewood, IL: Irwin.

57 Cumming, A., Wiltzius, P. & Bates, F. S. 1990 Nucleation and growth of monodisperse droplets in a binary-fluid system. *Phys. Rev. Lett.* **65**, 863–866. (doi:10.1103/PhysRevLett.65.863)

58 Jinnai, H., Nishikawa, Y., Koga, T. & Hashimoto, T. 1995 Direct observation of 3-dimensional bicontinuous structure developed via spinodal decomposition. *Macromolecules* **28**, 4782–4784. (doi:10.1021/ma00117a071)

59 Hashimoto, T., Hayashi, M. & Jinnai, H. 2000 Two-step phase separation of a polymer mixture. I. New scaling analysis for the main scattering peak. *J. Chem. Phys.* **112**, 6886–6896. (doi:10.1063/1.481317)

60 Förster, S., Timmann, A., Schellbach, C., Frömsdorf, A., Kornowski, A., Weller, H., Roth, S. V. & Lindner, P. 2007 Order causes secondary Bragg peaks in soft materials. *Nat. Mater.* **6**, 888–893. (doi:10.1038/nmat1995)

61 Dyck, J. 1992 Reflectance spectra of plumage areas colored by green feather pigments. *Auk* **109**, 293–301.

62 McComb, D. W., Treble, B. M., Smith, C. J., De La Rue, R. M. & Johnson, N. P. 2001 Synthesis and characterisation of photonic crystals. *J. Mater. Chem.* **11**, 142–148. (doi:10.1039/b003191g)

63 Mayoral, R. *et al.* 1997 3D long-range ordering in an SiO_2 submicrometer-sphere sintered superstructure. *Adv. Mater.* **9**, 257–260. (doi:10.1002/adma.19970090318)

64 Cardinaux, F., Gibaud, T., Stradner, A. & Schurtenberger, P. 2007 Interplay between spinodal decomposition and glass formation in proteins exhibiting short-range attractions. *Phys. Rev. Lett.* **99**, 118301. (doi:10.1103/Physrevlett.99.118301)

65 Stoddard, M. C. & Prum, R. O. 2008 Evolution of avian plumage color in a tetrahedral color space: a phylogenetic analysis of new world buntings. *Am. Nat.* **171**, 755–776. (doi:10.1086/587526)

66 Stoddard, M. C. & Prum, R. O. 2011 How colorful are birds? Evolution of the avian plumage color gamut. *Behav. Ecol.* **22**, 1042–1052. (doi:10.1093/Beheco/Arr088)

67 Hausmann, F., Arnold, K. E., Marshall, N. J. & Owens, I. P. F. 2003 Ultraviolet signals in birds are special. *Pro. R. Soc. Lond. B* **270**, 61–67. (doi:10.1098/rspb.2002.2200)

68 Hunt, S., Cuthill, I. C., Bennett, A. T. D., Church, S. C. & Partridge, J. C. 2001 Is the ultraviolet waveband a special communication channel in avian mate choice? *J. Exp. Biol.* **204**, 2499–2507.

69 Eaton, M. D. & Lanyon, S. M. 2003 The ubiquity of avian ultraviolet plumage reflectance. *Proc. R. Soc. Lond. B* **270**, 1721–1726. (doi:10.1098/rspb.2003.2431)

70 Fox, D. L. 1976 *Animal biochromes and structural colors.* Berkeley, CA: University California Press.

71 Prum, R. O. & Torres, R. H. 2003 Structural colouration of avian skin: convergent evolution of coherently scattering dermal collagen arrays. *J. Exp. Biol.* **206**, 2409–2429. (doi:10.1242/jeb.00431)

72 Stavenga, D. G., Tinbergen, J., Leertouwer, H. L. & Wilts, B. D. 2011 Kingfisher feathers—colouration by pigments, spongy nanostructures and thin films. *J. Exp. Biol.* **214**, 3960–3967. (doi:10.1242/Jeb.062620)

73 LaFountain, A. M., Kaligotla, S., Cawley, S., Riedl, K. M., Schwartz, S. J., Frank, H. A. & Prum, R. O. 2010 Novel methoxy-carotenoids from the burgundy-colored plumage of the pompadour cotinga xipholena punicea. *Arch. Biochem. Biophys.* **504**, 142–153. (doi:10.1016/j.abb.2010.08.006)

74 Burns, K. J. 1997 Molecular systematics of tanagers (Thraupinae): evolution and biogeography of a diverse radiation of neotropical birds. *Mol. Phylogenet. Evol.* **8**, 334–348. (doi:10.1006/mpev.1997.0430)

75 Garcia, P. D., Sapienza, R., Blanco, A. & Lopez, C. 2007 Photonic glass: a novel random material for light. *Adv. Mater.* **19**, 2597–2602. (doi:10.1002/adma.200602426)

76 Florescu, M., Torquato, S. & Steinhardt, P. J. 2009 Designer disordered materials with large, complete photonic band gaps. *Proc. Natl Acad. Sci. USA* **106**, 20 658–20 663. (doi:10.1073/pnas.0907744106)

77 Florescu, M., Torquato, S. & Steinhardt, P. J. 2009 Complete band gaps in two-dimensional photonic quasicrystals. *Phys. Rev. B* **80**, 155112. (doi:10.1103/Physrevb.80.155112)

78 Harun-Ur-Rashid, M., Bin Imran, A., Seki, T., Ishi, M., Nakamura, H. & Takeoka, Y. 2010 Angle-independent structural color in colloidal amorphous arrays. *Chemphyschem* **11**, 579–583. (doi:10.1002/cphc.200900869)

79 Lee, I. *et al.* 2010 Quasi-amorphous colloidal structures for electrically tunable full-color photonic pixels with angle-independency. *Adv. Mater.* **22**, 4973–4977. (doi:10.1002/adma.201001954)

80 Ueno, K., Inaba, A., Sano, Y., Kondoh, M. & Watanabe, M. 2009 A soft glassy colloidal array in ionic liquid, which exhibits homogeneous, non-brilliant and angle-independent structural colours. *Chem. Commun.* 3603–3605. (doi:10.1039/B905108b)

81 Parker, A. R. & Townley, H. E. 2007 Biomimetics of photonic nanostructures. *Nat. Nanotechnol.* **2**, 347–353. (doi:10.1038/nnano.2007.152)

82 Sanchez, C., Arribart, H. & Giraud Guille, M. M. 2005 Biomimetism and bioinspiration as tools for the design of innovative materials and systems. *Nat. Mater.* **4**, 277–288. (doi:10.1038/nmat1339)

83 Noh, H., Yang, J. K., Liew, S. F., Rooks, M. J., Solomon, G. S. & Cao, H. 2011 Control of lasing in biomimetic structures with short-range order. *Phys. Rev. Lett.* **106**, 183901. (doi:10.1103/Physrevlett.106.183901)